

The kaobook class

Use this document as a template

Multi-Messenger Observations of the Dynamic Universe

**Searching for sources of astrophysical neutrinos and gravitational
waves**

Robert Stein

May 18, 2020

An Awesome Publisher

The kaobook class

Disclaimer

You can edit this page to suit your needs. For instance, here we have a no copyright statement, a colophon and some other information. This page is based on the corresponding page of Ken Arroyo Ohori's thesis, with minimal changes.

No copyright

©@ This book is released into the public domain using the CC0 code. To the extent possible under law, I waive all copyright and related or neighbouring rights to this work.

To view a copy of the CC0 code, visit:

<http://creativecommons.org/publicdomain/zero/1.0/>

Colophon

This document was typeset with the help of KOMA-Script and L^AT_EX using the kaobook class.

The source code of this book is available at:

<https://github.com/fmarotta/kaobook>

THE CODE UseD TO PRODUCE PLOTS IN THis thesis can be found at...
(You are welcome to contribute!)

Publisher

First printed in May 2019 by An Awesome Publisher

A neutrino is not a big thing to be hit by.
In fact it's hard to think of anything much smaller by
which one could reasonably hope to be hit. And it's not as
if being hit by neutrinos was in itself a particularly
unusual event for something the size of the Earth. Far
from it. It would be an unusual nanosecond in which the
Earth was not hit by several billion passing neutrinos.

-The Hitchhiker's Guide to The Galaxy

Preface

I am of the opinion that every L^AT_EX geek, at least once during his life, feels the need to create his or her own class: this is what happened to me and here is the result, which, however, should be seen as a work still in progress. Actually, this class is not completely original, but it is a blend of all the best ideas that I have found in a number of guides, tutorials, blogs and tex.stackexchange.com posts. In particular, the main ideas come from two sources:

- ▶ Ken Arroyo Ohori's [Doctoral Thesis](#), which served, with the author's permission, as a backbone for the implementation of this class;
- ▶ The [Tufte-Latex Class](#), which was a model for the style.

The first chapter of this book is introductory and covers the most essential features of the class. Next, there is a bunch of chapters devoted to all the commands and environments that you may use in writing a book; in particular, it will be explained how to add notes, figures and tables, and references. The second part deals with the page layout and design, as well as additional features like coloured boxes and theorem environments.

I started writing this class as an experiment, and as such it should be regarded. Since it has always been intended for my personal use, it may not be perfect but I find it quite satisfactory for the use I want to make of it. I share this work in the hope that someone might find here the inspiration for writing his or her own class.

Federico Marotta

Detailed Contents

Preface	v
Detailed Contents	vi
1 Introduction	1
1.1 The Main Ideas	1
1.2 What This Class Does	1
1.3 What This Class Does Not Do	2
CLASS OPTIONS, COMMANDS AND ENVIRONMENTS	5
2 Class Options	7
2.1 KOMA Options	7
2.2 kao Options	7
2.3 Other Things Worth Knowing	8
2.4 Document Structure	8
3 Margin Stuff	11
3.1 Sidenotes	11
3.2 Marginnotes	11
3.3 Footnotes	12
3.4 Margintoc	12
4 Figures and Tables	13
4.1 Normal Figures and Tables	13
4.2 Margin Figures and Tables	14
4.3 Wide Figures and Tables	15
5 References	17
5.1 Citations	17
5.2 Glossaries and Indices	17
5.3 Hyperreferences	18
DESIGN AND ADDITIONAL FEATURES	21
6 Page Design	23
6.1 Headings	23
6.2 Headers & Footers	24
6.3 Table of Contents	24
6.4 Page Layout	25
6.5 Numbers & Counters	25
6.6 White Space	26
7 Mathematics and Boxes	27
7.1 Theorems	27
7.2 Boxes & Environments	28

7.3	Experiments	29
8	IceCube Neutrino Observatory	31
8.1	The IceCube Detector	31
8.2	Proposed Improvements to the IceCube detector	32
8.3	Detecting interactions in IceCube	33
8.4	Event Signatures	34
9	Event Selection and Reconstruction	35
9.1	Background Rejection	35
9.2	Muon Track Reconstruction	36
	LineFit	37
	SPE	37
	SplineMPE	37
	SegmentedSplineMPE	37
	Millipede	37
	DNN/RNN	38
9.3	Topological Classification	38
9.4	Energy Reconstruction	38
	MuEx	38
	Truncated Energy	38
9.5	Pull Corrections	38
9.6	Event Selection	39
	Cascade rejection	39
9.7	Systematic Errors	39
	Ice Models	39
	Detector Geometry	39
	Atmospheric Flux Uncertainties	39
	Pre-Pulses and After-Pulses	39
	Jitter	39
	DOM Efficiency	39
	HiveSplitter + Coincidence	39
	DOM Acceptance + Flasher Data	39
	Spline Tables/Resolution etc.	39
10	Sources of astrophysical neutrinos	41
10.1	Galactic Neutrino Emission	43
10.2	Emission from the Local Universe	44
10.3	Blazars	44
	TXS 0506+056	45
10.4	Gamma-Ray Bursts	46
10.5	Core-Collapse Supernova	47
10.6	Tidal Disruption Events (TDEs)	48
10.7	Fast Radio Bursts	50
10.8	Active Galactic Nuclei and Starburst Galaxies	50
11	Realtime Multi-Messenger Astronomy	53
11.1	The IceCube Realtime System	53
	IC160427A - The "PanSTARRS Supernova Neutrino"	54
	IC170922A The "TXS 0506+056 Neutrino"	55

IC190331A - The "Multi-PEV Neutrino"	55
IC190730A - The "PKS 1502+106 Neutrino"	55
IC190922B - The "SN2019pqh Neutrino"	56
IC191001A - The "Bran Stark Neutrino"	56
IC200107A - The "Flaring Extreme Blazar neutrino"	56
11.2 Interpreting high-energy neutrino alerts	56
Cluster searches	56
OFU and GFU	56
12 Transient Follow-up with ZTF	57
12.1 The AMPEL Follow-up Pipeline	57
12.2 Neutrino Follow-up	58
PKS 1502+106	60
SN2019pqh	60
12.3 Gravitational Waves and Gamma-ray Bursts	61
13 AT2019dsg and IC191001A	63
13.1 Discovery of AT2019dsg	63
13.2 Observation of AT2019dsg	64
Optical/UV	64
X-ray	65
Radio	66
Gamma-ray	69
Spectroscopy	70
13.3 Neutrino emission from AT2019dsg	72
13.4 Probability of Chance Coincidence	74
13.5 Implications of AT2019dsg	75
14 Overflow	77
14.1 Introduction	77
14.2 Neutrino Theory	78
14.3 The Zwicky Transient Facility (ZTF)	78
14.4 Event Selection	78
Event Reconstruction	78
Angular Errors	78
14.5 Unbinned Likelihood Analysis Formalism	78
14.6 Results	78
14.7 Diffuse Astrophysical Neutrino Flux	78
14.8 Neutrinos from Optical Transients	78
The Plot	78
14.9 Summary and Future Outlook	79
APPENDIX	81
A Heading on Level 0 (chapter)	83
A.1 Heading on Level 1 (section)	83
Heading on Level 2 (subsection)	83
A.2 Lists	84
Example for list (itemize)	84

Example for list (enumerate)	84
Example for list (description)	85
Bibliography	87
Alphabetical Index	93

Figures

1.1 The Mona Lisa	2
4.1 Mona Lisa, again	13
4.2 A wide seaside	15
10.1 The challenge of coherently understanding the scenarios for neutrino emission from blazars, given the two pieces of evidence from TXS 0506+056, as well as the constraints from IceCube stacking analyses, general point-source searches and generic time-dependent cluster searches. To date, no model has resolved all three observations coherently.	46
10.2 An overview of the current supernova classification scheme, which has been recently expanded to include superluminous supernova. Type 1a supernovae, marked in green, arise from thermonuclear explosions. All other classes, marked in orange, occur due to core collapse.	47
11.1 The archival SED of PKS 1502+106 from X is shown. In orange, the names of various instruments that observed the source are shown, with orange arrows to indicate their corresponding energy regimes. CITEA-Z	55
12.1 ZTF lightcurve of SN2019pqh, with observations in g and r band. The arrival time of the neutrino on 2019 September 22 is marked with a dotted line, and the supernova is detected in the subsequent ToO observations.	61
12.2 Spectrum of SN2019pqh, taken on x. The prominent Balmer lines are highlighted in orange, from which a redshift of 0.134 is derived. A template-matching classification using SNID yields a match to a Type I Ib supernova (SN1993J) 2 days before peak cite.	61
13.1 Multi-wavelength lightcurve of AT2019dsg. Error bars represent 1σ intervals. The upper panel shows the optical photometry from ZTF, alongside UV observations from <i>Swift</i> -UVOT. The plateau luminosity is a factor of 10 brighter in UVW2 than the pre-disruption baseline of the host galaxy. The lower panel shows the integrated X-ray energy flux, from observations with <i>Swift</i> -XRT and <i>XMM-Newton</i> , in the energy range 0.3-10 keV. Arrows indicated 3σ upper limits. The vertical dotted line illustrates the arrival of IC191001A.	64
13.2 X-ray count map from <i>XMM-Newton</i> (50 days after discovery). The green circle indicates the source region, while the red circular region was used to measure the background. The best-fit position derived from optical observations is spatially-coincident with the center of the X-ray source region.	66
13.3 Soft X-ray spectrum of AT2019dsg measured by <i>XMM-Newton</i> , fitted with an absorbed disk blackbody model. Error bars represent 1σ intervals.	67
13.4 LAT counts map of the Region Of Interest (ROI) in the integrated search period G3, showing the IC191001A 90% localisation region in green. The neutrino best-fit position is marked with a green ‘x’. Two gamma-ray sources are significantly detected ($\geq 5 \sigma$) in the ROI but outside the neutrino uncertainty region as marked with white crosses. There is no excess consistent with the position of AT2019dsg.	71

13.5 LAT lightcurve in the 0.1-800 GeV energy range for the source <i>Fermi</i> -J2113.8+1120 in the time interval G3, with evenly spaced binning of 28 days. Vertical error bars represent 1σ intervals, horizontal bars denote bin width. 2σ upper limits are shown for bins with $TS \leq 9$. The orange dashed vertical line marks the arrival time of IC-191001A. Since this source lies outside the reported 90% error region (see Figure 13.4), and given that the LAT lightcurve shows no obvious correlation with the neutrino arrival time, we conclude that it is unlikely to be associated with the neutrino.	71
13.6 The spectroscopic evolution of AT2019dsg, beginning with the publicly available classification spectrum taken with the NTT[2019ATel12752....1N], and further spectra from LDT, Lick, Keck and P200. The Balmer lines are highlighted in cyan, the HeII lines in gray, and the Bowen fluorescence lines (OIII at 3760Å, NIII at 4100Å and 4640Å) in black. Telluric lines are marked with +.	72

Tables

4.1 A useless table	14
4.2 Another useless table	15
6.1 Commands to add a particular entry to the table of contents.	25
12.1 Summary of the eight neutrino alerts followed up by ZTF, with IC191001A highlighted in bold. The 90% area column indicates the region of sky observed at least twice by ZTF, within the reported 90% localisation, and accounting for chip gaps. The <i>signalness</i> describes the probability that each neutrino is of astrophysical origin, rather than arising from atmospheric backgrounds. One alert, IC200107A, was reported without a signalness estimate.	59
12.2 Summary of the 23 neutrino alerts that were not followed up by ZTF since survey start on 2018 March 20. Of these, 4/23 were retracted, 11/23 were inaccessible to ZTF for various reasons, 6/23 were deemed alerts of poor quality, while just 2/23 were alerts that were missed although they passed our criteria.	60
13.1 Gamma-ray energy flux upper-limits for a point-source with power-law index $\Gamma=2.0$ at the position of AT2019dsg integrated over the analysis energy range 0.1-800 GeV.	70

Introduction

1.1 The Main Ideas¹

1.2 What This Class Does

1.3 What This Class Does Not Do

Many modern printed textbooks have adopted a layout with prominent margins where small figures, tables, remarks and just about everything else can be displayed. Arguably, this layout helps to organise the discussion by separating the main text from the ancillary material, which at the same time is very close to the point in the text where it is referenced.

This document does not aim to be an apology of wide margins, for there are many better suited authors for this task; the purpose of all these words is just to fill the space so that the reader can see how a book written with the kaobook class looks like. Meanwhile, I shall also try to illustrate the features of the class.

The main ideas behind kaobook come from this [blog post](#), and actually the name of the class is dedicated to the author of the post, Ken Arroyo Ohori, which has kindly allowed me to create a class based on his thesis. Therefore, if you want to know more reasons to prefer a 1.5-column layout for your books, be sure to read his blog post.

Another source of inspiration, as you may have noticed, is the [Tufte-Latex Class](#). The fact that the design is similar is due to the fact that it is very difficult to improve something which is already so good. However, I like to think that this class is more flexible than Tufte-Latex. For instance, I have tried to use only standard packages and to implement

1: ~~as little as possible from scratch~~ therefore, it should be pretty easy to ~~and contributing to the class development~~ customise anything, provided that you read the documentation of the ~~package that provides that feature~~.

~~you are interested, check out the repository on github!~~ In this book I shall illustrate the main features of the class and provide information about how to use and change things. Let us get started.

1.2 What This Class Does

The kaobook class focuses more about the document structure than about the style. Indeed, it is a well-known L^AT_EX principle that structure and style should be separated as much as possible (see also [Section 1.3 on the following page](#)). This means that this class will only provide commands, environments and in general, the opportunity to do things, which the user may or may not use. Actually, some stylistic matters are embedded in the class, but the user is able to customise them with ease.

The main features are the following:

2: This is another departure from Tufte's design.

3: Sidenotes (like this!) are numbered while marginnotes are not



Figure 1.1: The Mona Lisa.
[https://commons.wikimedia.org/
 wiki/File:Mona_Lisa,_by_Leonardo_da_Vinci,_from_C2RMF_retouched.jpg](https://commons.wikimedia.org/wiki/File:Mona_Lisa,_by_Leonardo_da_Vinci,_from_C2RMF_retouched.jpg)

Page Layout The text width is reduced to improve readability and make space for the margins, where any sort of elements can be displayed.

Chapter Headings As opposed to Tufte-Latex, we provide a variety of chapter headings among which to choose; examples will be seen in later chapters.

Page Headers They span the whole page, margins included, and, in twoside mode, display alternatively the chapter and the section name.²

Matters The commands `\frontmatter`, `\mainmatter` and `\backmatter` have been redefined in order to have automatically wide margins in the main matter, and narrow margins in the front and back matters. However, the page style can be changed at any moment, even in the middle of the document.

Margin text We provide commands `\sidenote` and `\marginnote` to put text in the margins.³

Margin figs/tabs A couple of useful environments is `marginfigure` and `marginable`, which, not surprisingly, allow you to put figures and tables in the margins (*cfr.* Figure 1.1).

Margin toc Finally, since we have wide margins, why don't add a little table of contents in them? See `\margintoc` for that.

Hyperref `hyperref` is loaded and by default we try to add bookmarks in a sensible way; in particular, the bookmarks levels are automatically reset at `\appendix` and `\backmatter`. Moreover, we also provide a small package to ease the hyperreferencing of other parts of the text.

Bibliography We want the reader to be able to know what has been cited without having to go to the end of the document every time, so citations go in the margins as well as at the end, as in Tufte-Latex. Unlike that class, however, you are free to customise the citations as you wish.

The order of the title pages, table of contents and preface can be easily changed, as in any L^AT_EX document. In addition, the class is based on KOMA-Script's `scrbook`, therefore it inherits all the goodies of that.

1.3 What This Class Does Not Do

As anticipated, further customisation of the book is left to the user. Indeed, every book may have sidenotes, margin figures and so on, but each book will have its own fonts, toc style, special environments and so on. For this reason, in addition to the class, we provide only sensible defaults, but if these features are not needed, they can be left out. These special packages are located in the `style` directory, which is organised as follows:

style.sty This package contains the specifications of page layout, headers and footers, chapter headings, and the fonts used throughout the document.

packages.sty Loads additional packages to decorate the writing with special contents (for instance, the `listing` package is loaded here

as it is not required in every book). There are also defined some useful commands to print the same words always in the same way, *e.g.* latin words in italics or packages in verbatim.

references.sty Some useful commands to manage labeling and referencing, again to ensure that the same elements are referenced always in a consistent way.

environments.sty Provides special environments, like boxes. Both simple and complex environments are available; by complex we mean that they are endowed with a counter, floating and can be put in a special table of contents.⁴

theorems.sty The style of mathematical environments. Acutally, there are two such packages: one is for plain theorems, *i.e.* the theorems are printed in plain text; the other uses `mdframed` to draw a box around theorems. You can plug the most appropriate style into its document.

In the rest of the book, I shall assume that the reader is not a novice in the use of L^AT_EX, and refer to the documentation of the packages used in this class for things that are already explained there. Moreover, I assume that the reader is willing to make minor edits to the provided packages for styles, environments and commands, if he or she does not like the default settings.

4: See [Chapter 7](#) on page 27 for some examples.

The audacious users might feel tempted to edit some of these packages. I'd be immensely happy if they sent me examples of what they have been able to do!

CLASS OPTIONS, COMMANDS AND ENVIRONMENTS

Class Options

2

In this chapter I will describe the most common options used, both the ones inherited from `scrbook` and the `kao`-specific ones. Options passed to the class modifies its default behaviour; beware though that some options may lead to unexpected results...

2.1 KOMA Options

The `kaobook` class is based on `scrbook`, therefore it understands all of the options you would normally pass to that class. If you have a lot of patience, you can read the KOMA-Script guide.⁶ Actually, the reading of such guide is suggested as it is very instructive.

Every KOMA-Script option you pass to the class when you load it is automatically activated. In addition, in `kaobook` some options have modified default values. For instance, the font size is 9.5pt and the paragraphs are separated by space,⁷ not marked by indentation.

2.2 kao Options

In the future I plan to add more options to set the paragraph formatting (justified or ragged) and the position of the margins (inner or outer in twoside mode, left or right in oneside mode).⁸

I take this opportunity to renew the call for help: everyone is encouraged to add features or reimplement existing ones, and to send me the results. You can find the GitHub repository at <https://github.com/fmarotta/kaobook>.

To Do

Implement the `justified` and `margin` options. To be consistent with the KOMA-Script style, they should accept a simple switch as a parameter, where the simple switch should be `true` or `false`, or one of the other standard values for simple switches supported by KOMA-Script. See the KOMA-Script documentation for further information.

The above box is an example of a `kaobox`, which will be discussed more thoroughly in Chapter 7 (Mathematics and Boxes) on page 27. Throughout the book I shall use these boxes to remarks what still needs to be done.

2.1 KOMA Options	7
2.2 kao Options	7
2.3 Other Things Worth Knowing	8
2.4 Document Structure	8

6: The guide can be downloaded from <https://ctan.org/pkg/koma-script?lang=en>.

7: To be precise, they are separated by half a line worth of space: the `parskip` value is ‘half’.

8: As of now, paragraphs are justified, formatted with `\singespacing` (from the `setspace` package) and `\frenchspacing`.

2.3 Other Things Worth Knowing

A bunch of packages are already loaded in the class because they are needed for the implementation. These include:

- ▶ etoolbox
- ▶ calc
- ▶ xifthen
- ▶ xkeyval
- ▶ xpars
- ▶ xstring

Many more packages are loaded, but they will be discussed in due time. Here, we will mention only one more set of packages, needed to change the paragraph formatting (recall that in the future there will be options to change this). In particular, the packages we load are:

- ▶ ragged2e
- ▶ setspace
- ▶ hyphenat
- ▶ microtype
- ▶ needspace
- ▶ xspace
- ▶ xcolor (with options `usenames`, `dvipsnames`)

Some of the above packages do not concern paragraph formatting, but we nevertheless grouped them with the others. By default, the main text is justified and formatted with singlespacing and frenchspacing; the margin text is the same, except that the font is a bit smaller.

2.4 Document Structure

We provide optional arguments to the `\title` and `\author` commands so that you can insert short, plain text versions of this fields, which can be used, typically in the half-title or somewhere else in the front matter, through the commands `\@plaintitle` and `\@plainauthor`, respectively. The PDF properties `pdftitle` and `pdfauthor` are automatically set by hyperref to the plain values if present, otherwise to the normal values.⁹

There are defined two page layouts, `margin` and `wide`, and two page styles, `plain` and `fancy`. The layout basically concern the width of the margins, while the style refers to headers and footer; these issues will be discussed in [Chapter 6 \(Page Design\) on page 23](#).¹⁰

The commands `\frontmatter`, `\mainmatter`, and `\backmatter` have been redefined in order to automatically change page layout and style for these sections of the book. The front matter uses the `margin` layout and the `plain` page style. In the `mainmatter` the margins are wide and the headings are fancy. In the appendix the style and the layout do not change; however we use `\bookmarksetup{startatroot}` so that the bookmarks of the chapters are on the root level (without this, they

9: We think that this is an important point so we remark it here. If you compile the document with pdflatex, the PDF metadata will be altered so that they match the plain title and author you have specified; if you did not specify them, the metadata will be set to the normal title and author.

10: For now, suffice it to say that pages with the `margin` layout have wide margins, while with the `wide` layout the margins are absent. In `plain` pages the headers and footer are suppressed, while in `fancy` pages there is a header.

would be under the preceding part). In the backmatter the margins shrink again and we also reset the bookmarks root.

3

Margin Stuff

Sidenotes are a distinctive feature of all 1.5-column-layout books. Indeed, having wide margins means that some material can be displayed there. We use margins for all kind of stuff: sidenotes, marginnotes, small tables of contents, citations, and, why not?, special boxes and environments.

3.1 Sidenotes

Sidenotes are like footnotes, except that they go in the margin, where they are more readable. To insert a sidenote, just use the command `\sidenote{Text of the note}`. You can specify a mark^O with `\sidenote[mark]{Text}`, but you can also specify an offset, which moves the sidenote upwards or downwards, so that the full syntax is:

```
\sidenote[offset][mark]{Text}
```

If you use an offset, you always have to add the brackets for the mark, but they can be empty.¹² The format of the actual sidenote can be changed with the command `\setsidenotes`, which allows you to modify, for instance, the format of the markers and the separator between the marker and the text of the sidenote.

There was an alternative package, `sidenotes`, which we could have used. In the end we went for `snotez` because it was the one used in Ken Ohori's thesis, which inspired this class. The features are very similar, but one additional thing offered by `snotez` is that the offset can be specified as a multiple of `\baselineskip`. For example, if you want to enter a sidenote with the normal mark and move it upwards one line, type:

```
\sidenote[*-1][] {Text of the sidenote.}
```

Sidenotes are handled through the `snotez` package, which in turn relies on the `marginnote` package.

3.2 Marginnotes

This command is very similar to the previous one. You can create a marginnote with `\marginnote[offset]{Text}`, where the offset argument can be left out, or it can be a multiple of `\baselineskip`, e.g.

```
\marginnote[-12pt]{Text} or \marginnote[-3]{Text}
```

3.1 Sidenotes	11
3.2 Marginnotes	11
3.3 Footnotes	12
3.4 Margintoc	12

O: This sidenote has a special mark, a big O!

12: If you want to know more about the usage of the `\sidenote` command, read the documentation of the `snotez` package.

While the command for margin notes comes from the `marginnote` package, it has been redefined in order to change the position of the optional offset argument, which now precedes the text of the note, whereas in the original version it was at the end. We have also added the possibility to use a multiple of `\baselineskip` as offset. These things were made only to make everything more consistent, so that you have to remember less things!

To Do

A small thing that needs to be done is to renew the `\sidenote` command so that it takes only one optional argument, the offset. The special mark argument can go somewhere else. In other words, we want the syntax of `\sidenote` to resemble that of `\marginnote`.

We load the packages `marginnote`, `marginfix` and `placeins`. Since `snotez` uses `marginnote`, what we said for `marginnotes` is also valid for `sidenotes`. Side- and margin- notes are shifted slightly upwards (`\renewcommand{\marginnotevadjust}{3pt}`) in order to allineate them to the bottom of the line of text where the note is issued.

3.3 Footnotes

Even though they are not displayed in the margin, we will discuss about footnotes here, since `sidenotes` are mainly intended to be a replacement of them. Footnotes force the reader to constantly move from one area of the page to the other. Arguably, `marginnotes` solve this issue, so you should not use footnotes. Nevertheless, for completeness, we have left the standard command `\footnote`, just in case you want to put a footnote once in a while.*

3.4 Margintoc

Since we are talking about margins, we introduce here the `\margintoc` command, which allows one to put small table of contents in the margin. Like other commands we have discussed, `\margintoc` accepts a parameter for the vertical offset, like so: `\margintoc[offset]`.

The command can be used in any point of the document, but we think it makes sense to use it just at the beginning of chapters or parts. In this document I make use of a KOMA-Script feature and put it in the chapter preamble, with the following code:

```
\setchapterpreamble[u]{\margintoc}
\chapter{Chapter title}
```

Not only textual stuff can be displayed in the margin, but also figures. Those will be the focus of the next chapter.

The font used in the `margintoc` is the same as the one for the chapter entries in the main table of contents at the beginning of the document.

* And this is how they look like. Notice that in the PDF file there is a back reference to the text; pretty cool, uh?



4 Figures and Tables

4.1 Normal Figures and Tables

Figures and tables can be inserted just like in any standard L^AT_EX document. The `graphicx` package is already loaded and configured in such a way that the figure width is equal to the `textwidth` and the height is adjusted in order to maintain the original aspect ratio. As you may have imagined, the captions will be positioned... well, in the margins. This is achieved with the help of the `floatrow` package.

Here is a picture of Mona Lisa ([Figure 4.1](#)), as an example. The captions are formatted as the margin- and the side-notes; If you want to change something about captions you can use the command `\captsetup` from the `caption` package. Remember that if you want to reference a figure, the label must come *after* the caption!



4.1 Normal Figures and Tables	13
4.2 Margin Figures and Tables	14
4.3 Wide Figures and Tables . .	15

Figure 4.1: It's Mona Lisa again. Hello, here is some text without a meaning. This text should show what a printed text will look like at this place. If you read this text, you will get no information. Really? Is there no information? Is there a difference between this text and some nonsense like "Huardest gefburn"? Kjift – not at all! A blind text like this gives you information about the selected font, how the letters are written and an impression of the look. This text should contain all letters of the alphabet and it should be written in of the original language. There is no need for special content, but the length of words should match the language.

While the format of the caption is managed by `caption`, its position is handled by the `floatrow` package. Achieving this result has been quite hard, but now I am pretty satisfied. In two-side mode, the captions are printed in the correct margin.

Tables can be inserted just as easily as figures, as exemplified by the following code:

```

1 \begin{table}
2 \begin{tabular}{ c c c c }
3   \toprule
4   col1 & col2 & col3 & col 4 \\
5   \midrule
6   \multirow{3}{4em}{Multiple row} & cell2 & cell3 & cell4\\ &
7   cell5 & cell6 & cell7 \\ &
8   cell8 & cell9 & cell10 \\
9   \multirow{3}{4em}{Multiple row} & cell2 & cell3 & cell4 \\ &
10  cell5 & cell6 & cell7 \\ &
11  cell8 & cell9 & cell10 \\
12  \bottomrule
13 \end{tabular}
14 \end{table}
```

which results in the useless [Table 4.1](#).

Table 4.1: A useless table.

	col1	col2	col3	col 4
Multiple row	cell2	cell3	cell4	
	cell5	cell6	cell7	
	cell8	cell9	cell10	
Multiple row	cell2	cell3	cell4	
	cell5	cell6	cell7	
	cell8	cell9	cell10	

I don't have much else to say, so I will just insert some blind text. Hello, here is some text without a meaning. This text should show what a printed text will look like at this place. If you read this text, you will get no information. Really? Is there no information? Is there a difference between this text and some nonsense like "Huardest gefburn"? Kjift – not at all! A blind text like this gives you information about the selected font, how the letters are written and an impression of the look. This text should contain all letters of the alphabet and it should be written in of the original language. There is no need for special content, but the length of words should match the language.

4.2 Margin Figures and Tables

Marginfigures can be inserted with the environment `marginfigure`. In this case, the whole picture is confined to the margin and the caption is below it. [Figure 1.1](#) is obtained with something like this:

```

1 \begin{marginfigure}
2   \includegraphics{monalisa}
3   \caption[The Mona Lisa]{The Mona Lisa.}
4   \labfig{marginmonalisa}
```

```
5 | \end{marginfigure}
```

There is also the `marginable` environment, of which [Table 4.2](#) is an example. Notice how you can place the caption above the table by just placing the `\caption` command before beginning the `tabular` environment. Usually, figure captions are below, while table captions are above. This rule is also respected for normal figures and tables: the captions are always on the side, but for figure they are aligned to the bottom, while for tables to the top.

Marginfigures and tables can be positioned with an optional offset command, like so:

```
1 | \begin{marginfigure}[offset]
2 |   \includegraphics{images/seaside}
3 | \end{marginfigure}
```

Offset can be either a measure or a multiple of `\baselineskip`, much like with `\sidenote`, `\marginnote` and `\margintoc`. If you are wondering how I inserted this orange bubble, have a look at the `todo` package.

Table 4.2: Another useless table.

col1	col2	col3
Multiple	cell2	cell3
row	cell5	cell6
	cell8	cell9

Improve this part.

4.3 Wide Figures and Tables



Figure 4.2: A wide seaside, and a wide caption. Credits: By Bushra Feroz — Own work, CC BY-SA 4.0, <https://commons.wikimedia.org/w/index.php?curid=68724647>

With the environments `figure*` and `table*` you can insert figures which span the whole page width. The caption will be positioned below or above, according to taste.

You may have noticed the full width image at the very beginning of this chapter: that, however, is set up in an entirely different way, which you'll read about in [Chapter 6 on page 23](#). Now it is time to tackle hyperreferences.

5.1 Citations

To cite someone [Visscher2008, James2013] is very simple: just use the `\sidecite` command. It does not have an offset argument yet, but it probably will in the future. This command supports multiple entries, as you can see, and by default it prints the reference on the margin as well as adding it to the bibliography at the end of the document. For this setup I used biblatex but I think that workarounds are possible.[James2013] Note that the citation [James2013]: in the margin [James2013], with the text, they are completely random as they only serve the purpose to illustrate the feature.

[Visscher2008]:
 (Visscher2008), Visscher2008
 [James2013]: James2013
 James2013

To compile a document containing citations, you need to use an external tool, which for this class is biber. You need to run the following (assuming that your tex file is called `main.tex`):

```
$ pdflatex main
$ biber main
$ pdflatex main
```

5.2 Glossaries and Indices

The `kaobook` class loads the packages `glossaries` and `imakeidx`, with which you can add glossaries and indices to your book. For instance, I previously defined some glossary entries and now I am going to use them, like this: `computer`. `glossaries` also allows you to use acronyms, like the following: this is the full version, `Frame per Second (FPS)`, and this is the short one `FPS`. These entries will appear in the glossary in the backmatter.

Unless you use `Overleaf` or some other fancy IDE for L^AT_EX, you need to run an external command from your terminal in order to compile a document with a glossary. In particular, the commands required are.¹⁵

```
$ pdflatex main
$ makeglossaries main
$ pdflatex main
```

Note that you need not run `makeglossaries` every time you compile your document, but only when you change the glossary entries.

To create an index, you need to insert the command `\index{subject}` whenever you are talking about ‘subject’ in the text. For instance, at the start of this paragraph I would write `\index{index}`, and an entry would be added to the Index in the backmatter. Check it out!

¹⁵: These are the commands you would run in a UNIX system; I have no idea on how it works in Windows.

In theory, you would need to run an external command for the index as well, but luckily the package we suggested, `imakeidx`, can compile the index automatically.

A nomenclature is just a special kind of index; you can find one at the end of this book. To insert a nomenclature, we use the package `nomencl` and add the terms with the command `\nomenclature`. We put then a `\printnomenclature` where we want it to appear.

Also with this package we need to run an external command to compile the document, otherwise the nomenclature will not appear:

```
$ pdflatex main
$ makeindex main.nlo -s nomencl.ist -o main.nls
$ pdflatex main
```

These packages are all loaded in `packages.sty`, one of the files that come with this class. However, the configuration of the elements is best done in the `main.tex` file, since each book will have different entries and styles.

This brief section was by no means a complete reference on the subject, therefore you should consult the documentation of the above package to gain a full understanding of how they work.

Note that the `nomencl` package caused problems when the document was compiled, so, to make a long story short, I had to prevent `scrhack` to load the hack-file for `nomencl`. When compiling the document on Overleaf, however, this problem seem to vanish.

5.3 Hyperreferences

In this class we provide a handy sub-package to help you referencing the same elements always in the same way, for consistency across the book. First, you can label each element with a specific command. For instance, should you want to label a chapter, you would put `\labch{chapter-title}` right after the `\chapter` directive. This is just a convenience, because `\labch` is actually just an alias to `\label{ch:chapter-title}`, so it spares you the writing of 'ch'. We defined similar commands for many typically labeled elements, including:

- | | |
|--|---|
| <ul style="list-style-type: none"> ▶ Page: <code>\labpage</code> ▶ Part: <code>\labpart</code> ▶ Chapter: <code>\labch</code> ▶ Section: <code>\labsec</code> ▶ Figure: <code>\labfig</code> ▶ Table: <code>\labtab</code> ▶ Definition: <code>\labdef</code> | <ul style="list-style-type: none"> ▶ Theorem: <code>\labthm</code> ▶ Proposition: <code>\labprop</code> ▶ Lemma: <code>\lablemma</code> ▶ Remark: <code>\labremark</code> ▶ Example: <code>\labexample</code> ▶ Exercise: <code>\labexercise</code> |
|--|---|

Of course, we have similar commands for referencing those elements. However, since the style of the reference should depend on the context, we provide different commands to reference the same thing. For instance, in some occasions you may want to reference the chapter by name, but other times you want to reference it only by number. In general, there are four reference style, which we call plain, vario, name, and full.

The plain style references only by number. It is accessed, for chapters, with `\refch{chapter-title}` (for other elements, the syntax is analogous). Such a reference results in: [Chapter 5](#).

The vario and name styles rest upon the varioref package. Their syntax is `\vrefch{chapter-title}` and `\nrefch{chapter-title}`, and they result in: [Chapter 5 on page 17](#), for the vario style, and: [Chapter 5 \(References\)](#), for the name style. As you can see, the page is referenced in varioref style.

The full style references everything. You can use it with `\frefch{chapter-title}` and it looks like this: [Chapter 5 \(References\) on page 17](#).

Of course, all the other elements have similar commands (*e.g.* for parts you would use `\vrefpart{part-title}` or something like that). However, not all elements implement all the four styles. The commands provided should be enough, but if you want to see what is available or to add the missing ones, have a look at the [attached package](#).

DESIGN AND ADDITIONAL FEATURES



6 Page Design

6.1 Headings

So far, in this document I used two different styles for the chapter headings: one has the chapter name, a rule and, in the margin, the chapter number; the other has an image at the top of the page, and the chapter title is printed in a box (like for this chapter). There is one additional style, which I used only in the appendix (on page 83); there, the chapter title is enclosed in two horizontal rules, and the chapter number (or letter, in the case of the appendix) is above it.¹⁷

Every book is unique, so it makes sense to have different styles from which to choose. Actually, it would be awesome if whenever a kao-user designs a new heading style, he or she added it to the three styles already present, so that it will be available for new users and new books.

The choice of the style is made simple by the `\setchapterstyle` command. It accepts one option, the name of the style, which can be: ‘plain’, ‘kao’, or ‘lines’.¹⁸ If instead you want the image style, you have to use the command `\setchapterimage`, which accepts the path to the image as argument; you can also provide an optional parameter in square brackets to specify the height of the image.

Let us make some examples. In this book, I begin a normal chapter with the lines:

```
1 | \setchapterstyle{kao}
2 | \setchapterpreamble[u]{\marginintoc}
3 | \chapter{Title of the Chapter}
4 | \labch{title}
```

In Line 1 I choose the style for the title to be ‘kao’. Then, I specify that I want the margin toc. The rest is ordinary administration in L^AT_EX, except that I use my own `\labch` to label the chapter. Actually, the `\setchapterpreamble` is a standard KOMA-Script one, so I invite you to read about it in the KOMA documentation. Once the chapter style

6.1 Headings	23
6.2 Headers & Footers	24
6.3 Table of Contents	24
6.4 Page Layout	25
6.5 Numbers & Counters	25
6.6 White Space	26

17: To be honest, I do not think that mixing heading styles like this is a wise choice, but in this document I did only to show you how they look.

18: Plain is the default L^AT_EX title style; the other ones are self explanatory.

19: The `\margintoc` has to be specified at every chapter. Perhaps in the future this may change; it all depends on how this feature will be welcomed by the users, so keep in touch with me if you have preferences!

is set, it holds until you change it.¹⁹ Whenever I want to start a chapter with an image, I simply write:

```

1 \setchapterimage[7cm]{path/to/image.png} % Optionally specify the
   height
2 \setchapterpreamble[u]{\margintoc}
3 \chapter{Catchy Title} % No need to set a chapter style
4 \labch{catchy}
```

6.2 Headers & Footers

Headers and footers in KOMA-Script are handled by the `scrlayer-scrpage` package. There are two basic style: ‘`scrheadings`’ and ‘`plain.scrheadings`’. The former is used for normal pages, whereas the latter is used in title pages (those where a new chapter starts, for instance) and, at least in this book, in the front matter. At any rate, the style can be changed with the `\pagestyle` command, *e.g.* `\pagestyle{plain.scrheadings}`.

In both styles, the footer is completely empty. In `plain.scrheadings`, also the header is absent (otherwise it wouldn’t be so plain...), but in the normal style the design is reminiscent of the ‘`kao`’ style for chapter titles.

To Do

The `twoside` class option is still unstable and. As always, any help will be greatly appreciated.

6.3 Table of Contents

Another important part of a book is the table of contents. By default, in `kaobook` there is an entry for everything: list of figures, list of tables, bibliographies, and even the table of contents itself. Not everybody might like this, so we will provide a description of the changes you need to do in order to enable or disable each of these entries. In the following [Table 6.1](#), each item corresponds to a possible entry in the `TOC`, and its description is the command you need to provide to have such entry. These commands are specified in the attached `style package`,²⁰ so if you don’t want the entries, just comment the corresponding lines.

20: In the same file, you can also choose the titles of these entries.

In a later section, we will see how you can define your own floating environment, and endow it with an entry in the `TOC`.

Of course, some packages, like those for glossaries and indices, will try to add their own entries. In such cases, you have to follow the instructions specific to that package. Here, since we have talked about glossaries and notations in [Chapter 5](#), we will briefly see how to configure them.

For the `glossaries` package, use the ‘`toc`’ option when you load it: `\usepackage[toc]{glossaries}`. For `nomencl`, pass the ‘`intoc`’ option at the moment of loading the package. Both `glossaries` and `nomencl` are loaded in the attached ‘`packages`’ package.

Entry	Command to Activate
Table of Contents	\setuptoc{toc}{totoc}
List of Figs and Tabs	\PassOptionsToClass{toc=listof}{\@baseclass}
Bibliography	\PassOptionsToClass{toc=bibliography}{\@baseclass}

Table 6.1: Commands to add a particular entry to the table of contents.

Additional configuration of the table of contents can be performed through the packages `etoc`, which is loaded because it is needed for the `margintocs`, or the more traditional `tocbase`. Read the respective documentations if you want to be able to change the default `TOC` style.²¹

21: (And please, send me a copy of what you have done, I'm so curious!)

6.4 Page Layout

Besides the page style, you can also change the width of the content of a page. This is particularly useful for pages dedicated to part titles, where having the 1.5-column layout might be a little awkward, or for pages where you only put figures, where it is important to exploit all the available space.

In practice, there are two layouts: ‘wide’ and ‘margin’. The former suppresses the margins and allocates the full page for contents, while the latter is the layout used in most of the pages of this book, including this one. The wide layout is also used automatically in the front and back matters.

To change page layout, use the `\pagelayout` command. For example, when I start a new part, I write:

```

1 \pagelayout{wide}
2 \addpart{Title of the New Part}
3 \pagelayout{margin}
```

6.5 Numbers & Counters

In this short section we shall see how dispositions, sidenotes and figures are numbered in the `kaobook` class.

By default, dispositions are numbered up to the section. This is achieved by setting: `\setcounter{secnumdepth}{1}`.

The sidenotes counter is the same across all the document, but if you want it to reset at each chapter, just uncomment the line

```
\counterwithin*{sidenote}{chapter}
```

in the `styles/style.sty` package provided by this class.

Figure and Table numbering is also per-chapter; to change that, use something like:

```
\renewcommand{\thefigure}{\arabic{section}.\arabic{figure}}
```

6.6 White Space

One of the things that I find most hard in L^AT_EX is to finely tune the white space around objects. There are not fixed rules, each object needs its own adjustment. Here we shall see how some spaces are defined at the moment in this class.

Attention! This section may be incomplete.

Space around figures and tables

```
\renewcommand\FBskip{.4\topskip}  
\renewcommand\FBbskip{\FBskip}
```

Space around captions

```
\captionsetup{  
    aboveskip=6pt,  
    belowskip=6pt  
}
```

Space around displays (e.g. equations)

```
\setlength\abovedisplayskip{6pt plus 2pt minus 4pt}  
\setlength\belowdisplayskip{6pt plus 2pt minus 4pt}  
\abovedisplayskip 10\p@ \oplus2\p@ \minus5\p@  
\abovedisplayshortskip \z@ \oplus3\p@  
\belowdisplayskip \abovedisplayskip  
\belowdisplayshortskip 6\p@ \oplus3\p@ \minus3\p@
```

7.1 Theorems

Despite most people complain at the sight of a book full of equations, mathematics is an important part of many books. Here, we shall illustrate some of the possibilities. We believe that theorems, definitions, remarks and examples should be emphasised with a shaded background; however, the colour should not be too heavy on the eyes, so we have chosen a sort of light yellow.²³

Definition 7.1.1 Let (X, d) be a metric space. A subset $U \subset X$ is an open set if, for any $x \in U$ there exists $r > 0$ such that $B(x, r) \subset U$. We call the topology associated to d the set τ_d of all the open subsets of (X, d) .

Definition 7.1.1 is very important. I am not joking, but I have inserted this phrase only to show how to reference definitions. The following statement is repeated over and over in different environments.

Theorem 7.1.1 A finite intersection of open sets of (X, d) is an open set of (X, d) , i.e τ_d is closed under finite intersections. Any union of open sets of (X, d) is an open set of (X, d) .

Proposition 7.1.2 A finite intersection of open sets of (X, d) is an open set of (X, d) , i.e τ_d is closed under finite intersections. Any union of open sets of (X, d) is an open set of (X, d) .

Lemma 7.1.3 A finite intersection^a of open sets of (X, d) is an open set of (X, d) , i.e τ_d is closed under finite intersections. Any union of open sets of (X, d) is an open set of (X, d) .

^a I'm a footnote

You can safely ignore the content of the theorems... I assume that if you are interested in having theorems in your book, you already know something about the classical way to add them. These example should just showcase all the things you can do within this class.

Corollary 7.1.4 (Finite Intersection, Countable Union) A finite intersection of open sets of (X, d) is an open set of (X, d) , i.e τ_d is closed under finite intersections. Any union of open sets of (X, d) is an open set of (X, d) .

Proof. The proof is left to the reader as a trivial exercise. Hint: Hello, here is some text without a meaning. This text should show what a printed text will look like at this place. If you read this text, you will get no information. Really? Is there no information? Is there a difference

7.1 Theorems	27
7.2 Boxes & Environments	28
7.3 Experiments	29

23: The boxes are all of the same colour here, because we did not want our document to look like Harlequin.

You can even insert footnotes inside the theorem environments; they will be displayed at the bottom of the box.

between this text and some nonsense like “Huardest gefburn”? Kjift – not at all! A blind text like this gives you information about the selected font, how the letters are written and an impression of the look. This text should contain all letters of the alphabet and it should be written in of the original language. There is no need for special content, but the length of words should match the language. \square

Here is a random equation, just because we can:

$$x = a_0 + \cfrac{1}{a_1 + \cfrac{1}{a_2 + \cfrac{1}{a_3 + \cfrac{1}{a_4}}}}$$

Definition 7.1.2 Let (X, d) be a metric space. A subset $U \subset X$ is an open set if, for any $x \in U$ there exists $r > 0$ such that $B(x, r) \subset U$. We call the topology associated to d the set τ_d of all the open subsets of (X, d) .

Example 7.1.1 Let (X, d) be a metric space. A subset $U \subset X$ is an open set if, for any $x \in U$ there exists $r > 0$ such that $B(x, r) \subset U$. We call the topology associated to d the set τ_d of all the open subsets of (X, d) .

Remark 7.1.1 Let (X, d) be a metric space. A subset $U \subset X$ is an open set if, for any $x \in U$ there exists $r > 0$ such that $B(x, r) \subset U$. We call the topology associated to d the set τ_d of all the open subsets of (X, d) .

As you may have noticed, definitions, example and remarks have independent counters; theorems, propositions, lemmas and corollaries share the same counter.

Remark 7.1.2 Here is how an integral looks like inline: $\int_a^b x^2 dx$, and here is the same integral displayed in its own paragraph:

$$\int_a^b x^2 dx$$

We provide two files for the theorem styles: `plaintheorems.sty`, which you should include if you do not want coloured boxes around theorems; and `mdftheorems.sty`, which is the one used for this document.²⁴ Of course, you will have to edit these files according to your taste and the general style of the book.

24: The plain one is not showed, but actually it is exactly the same as this one, only without the yellow boxes.

7.2 Boxes & Custom Environments²⁵

25: Notice that in the table of contents and in the header, the name of this section is ‘Boxes & Environments’; we achieved this with the optional argument of the `section` command.

Say you want to insert a special section, an optional content or just something you want to emphasise. We think that nothing works better than a box in these cases. We used `mdframed` to construct the ones shown below. You can create and modify such environments by editing the provided file `environments.sty`.

Title of the box
Hello, here is some text without a meaning. This text should show what a printed text will look like at this place. If you read this text, you will get no information. Really? Is there no information?

Is there a difference between this text and some nonsense like "Huardest gefburn"? Kjift – not at all! A blind text like this gives you information about the selected font, how the letters are written and an impression of the look. This text should contain all letters of the alphabet and it should be written in of the original language. There is no need for special content, but the length of words should match the language.

If you set up a counter, you can even create your own numbered environment.

Comment 7.2.1

Hello, here is some text without a meaning. This text should show what a printed text will look like at this place. If you read this text, you will get no information. Really? Is there no information? Is there a difference between this text and some nonsense like "Huardest gefburn"? Kjift – not at all! A blind text like this gives you information about the selected font, how the letters are written and an impression of the look. This text should contain all letters of the alphabet and it should be written in of the original language. There is no need for special content, but the length of words should match the language.

7.3 Experiments

It is possible to wrap marginnotes inside boxes, too. Audacious readers are encouraged to try their own experiments and let me know the outcomes.

I believe that many other special things are possible with the kaobook class. During its development, I struggled to keep it as flexible as possible, so that new features could be added without too great an effort. Therefore, I hope that you can find the optimal way to express yourselves in writing a book, report or thesis with this class, and I am eager to see the outcomes of any experiment that you may try.

title of margin note

Margin note inside a kaobox.
(Actually, kaobox inside a margin-note!)



8 IceCube Neutrino Observatory

// I am hell-bent for the South Pole — God willing and crevasses permitting. //

Edmund Hillary, , 1957

8.1 The IceCube Detector	31
8.2 Proposed Improvements to the IceCube detector	32
8.3 Detecting interactions in IceCube	33
8.4 Event Signatures	34

The IceCube Neutrino Observatory is the world’s largest neutrino telescope, located at the geographic south pole. It was built as a successor to the AMANDA experiment, which had pioneered the detection of neutrinos in ice. AMANDA served as a proof of concept for the detection of neutrinos, but with a volume of just nm^3 , it only had sufficient effective area to measure atmospheric neutrinos.

IceCube, on the other hand, was envisioned as a much larger detector capable of measuring astrophysical neutrinos. It was constructed in phases from 2006 to 2011, eventually reaching a total volume of one cubic kilometer.

8.1 The IceCube Detector

IceCube is composed of 86 strings arranged in a hexagonal grid. Each string is 2.5 km long, and carries regularly-spaced Digital Optical Modules (DOMs) containing Photo-Multiplier Tubes (PMTs). With a hot-water drill, holes were drilled into the glacier ice to a depth of 2.5 km. After string deployment, the liquid-filled holes refroze, fixing the DOMs in place. In total, there are 5160 DOMs deployed in IceCube, all at depths greater than 1km. The Antarctic ice itself thus provides the detection medium for neutrinos, with the Earth acting as a shield against atmospheric muons.

The design of IceCube is an optimisation trading DOM-density against effective area for fixed cost. A minimal DOM density is needed to

identify and reconstruct an event, and this threshold decreases as neutrino energy increases. Thus, while IceCube is generally optimised for detecting high-energy neutrinos in the astrophysical regime, it is far too sparse to effectively measure lower-energy (1-100 GeV) neutrinos. However, in addition to the regular grid of strings, IceCube contains a denser in-fill array known as *Deepcore*. This array consists of 7 strings and n DOMs, and typically uses the outer IceCube detector as a veto against muons?. *Deepcore* measures low-energy neutrinos which form the basis of neutrino oscillation studies, but can also be used for neutrino astronomy at lower energy scales.

IceCube also contains a surface array of instrumented ice tanks known as IceTop, which are used to measure surface air showers arising from cosmic rays and photon interactions. IceTop can be used as a veto against muons from air showers, but only for a small fraction of events which are almost-vertically down-going. However, IceTop also functions in its own right as a Cosmic-Ray detector, and contributes competitive measurements of the cosmic ray flux and composition.

While most event selections for GeV and TeV-PeV neutrinos require multiple DOM hits to reject thermal-noise background, a separate detection channel exists for MeV neutrinos that are typically produced in both stellar fusion and supernova collapse. These neutrinos form an irreducible background for the IceCbe detector, with extremely short track lengths that are only detectable by single DOMs. A dedicated SuperNova Data Aquistion System (SNDAQ) is installed to measure the rate of these single-DOM detections, and identify any significant deviation from expected rates. As demonstrated by SN1987a, any nearby supernova will produce a significant flux of MeV neutrinos during core collapse, and this will be manifested in a significant uptick in trigger rate that will evolve as a function of time. It is predicted that IceCube will be able to clearly measure the temporal evolution of MeV neutrinos from any supernova in the galaxy or Magellanic Clouds, similar to Figure NNNN. IceCube sends any mid-significance deviations from trigger rate to the SuperNova Early Warning System (SNEWS), where they are cross-correlated with other sensitive neutrino detectors such as SNO and Super-K. In the event of a multi-detector trigger, observatories around the world will be alerted to the upcoming optical counterpart of a galactic supernova, which can be localised in the case of a strong signal by combining directional information from individual detectors and time-delays between detectors in differing geographical locations.

MeV neutrinos for supernovae.

8.2 Proposed Improvements to the IceCube detector

There are several planned or proposed extensions to IceCube that would substantially improve the detector performance. Beginning in 2023, deployment will start for the IceCube Upgrade, a Deepcore-like

dense infill array. The string spacing will be even tighter than deep-core, with a higher density of DOMs. In combination with hardware improvements from multi-PMT DOMs, the Upgrade should push IceCube's lower energy threshold from a few GeV, and potentially to below one GeV. This opens up an entirely new regime for both oscillation studies and lower-energy neutrino astronomy relative to competitor neutrino detectors such as SuperK. In addition to the gains from DOMs, many new calibration devices will be deployed to more accurately constrain sources of systematic uncertainties, in particular the ice scattering and absorption length. With these calibration measurements, archival neutrino data can be reprocessed, providing more accurate reconstructed parameters. Improvement should be expected for all neutrino sources analyses, which all suffer to lesser or greater degree from these systematic errors.

Beyond the IceCube Upgrade, a more comprehensive improvement is planned to extend the higher-energy capability of IceCube. IceCube-Gen2 is a proposed extension instrumenting 10 km³ of ice, with a sparser string footprint than the existing detector. While multi-PMT DOMs should partially compensate the lower density, Gen2 represents a transition in focus to higher-energy neutrinos at 10TeV-100PeV range, at the cost of poorer resolution for lower-energy neutrinos with few DOM hits. Given the tenfold increase in instrumented volume, IceCube Gen2 will substantially increase sensitivity to both steady and time-dependent neutrino sources.

A further radio-based extension is proposed to complement the DOM-based Gen2 component. The detection of radio-based air shower detection has been demonstrated by the Pierre Auger Observatory, and its use in ice was pioneered by the ARA and ARIANNA collaborations. A pilot array for neutrino detection is currently being deployed in Greenland. Radio-based observatories are cheap, and given the possibility of single-station shower detection, an extremely sparse array can be deployed to substantially boost effective area. The proposed radio-based component for Gen2, covering n000 stations, would significantly improve sensitivity at the higher energies beyond nPeV, and could additionally probe the cosmogenic neutrino flux produced by interactions of UHECRs and CMB photons.

IceAct?

8.3 Detecting interactions in IceCube

Neutrinos are indirectly detected in IceCube via charged secondary particles produced through interactions in the ice. These daughter particles, arising from both CC and NC interactions, emit via the Cherenkov effect when travelling faster than the local speed of light in ice. The light is emitted at a characteristic Cherenkov Angle, θ_c , determined by the refractive index in ice and the particle velocity:

$$\theta_c = \frac{1}{\eta\beta}$$

These Cherenkov photons travel through the ice, and can then be detected by one or more DOMs. During propagation, these photons can be both scattered or absorbed by the ice, which is somewhat inhomogeneous. In particular, there is a substantial layer of dust spanning the central depth range of the detector, and scattering is consequently elevated in this region.

Basic Triggers

Waveform saving

Digitisation

8.4 Event Signatures

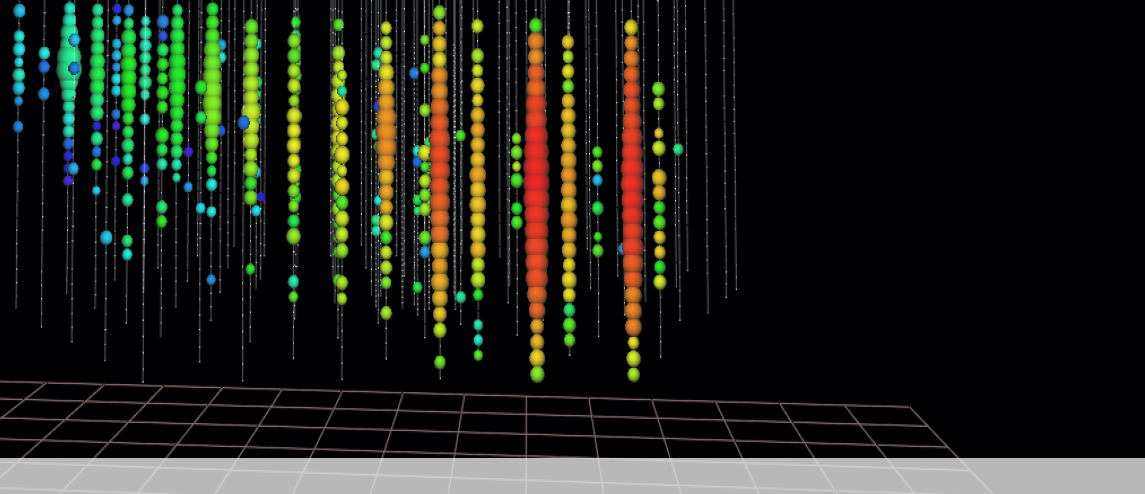
There are two standard event topologies that IceCube sees, namely Tracks and Cascades. Charged-current muon-neutrino interactions produce muons, which then typically traverses the detector while ionising the ice, result is a track-like event. These tracks typically have well-reconstructed positions, because the kilometer-scale lever arm can typically constrain the direction well. However, by virtue of the outgoing muon leaving the detector, these events typically have poor energy resolution.

Charged-current electron-neutrino interactions, as well as neutral-current interactions of all flavours, instead produce cascade-like particle showers in the detector. In these cases, light propagates approximately spherically from the interaction vertex, resulting in a poor angular resolution of order 10 degrees. However, as the light is typically contained by the detector, IceCube can act as a calorimeter and constrain the neutrino energy with a resolution of n%.

Charged-current tau-neutrino interactions lead to the production of a tau with various possible signatures. In 17% of interactions, a track-like signature will be created through a XXX. Additionally, a tau neutrino can produce a unique Double-Bang signature. Here one cascade is produced alongside a tau, which then propagates through the ice before decaying to an electron and producing a second cascade. The separation between these cascades, L_{DC} will vary depending on the degree of length contraction experienced for the tau before decay, and is thus roughly proportional to energy:

$$L_{DC} \approx \frac{E_\nu}{1PeV} \times 1m$$

Given the DOM spacing in IceCube, a minimal tau energy of approximately n00TeV is required for such events to be identified. The vast majority of tau-neutrino interactions will be indistinguishable from cascades for IceCube's resolution. The three topologies are illustrated in Figure N.



9 Event Selection and Reconstruction

// Sometimes science is more art than science //

Rick Sanchez, *Rick and Morty*, 20xx

The geometry of the IceCube detector is non-isotropic, and this leads to a zenith-dependence in both effective area and background. As a consequence of IceCube's location at the South Pole, zenith can be linearly mapped to declination, leading to a significantly declination-dependent sensitivity for all neutrino fluxes. In addition, for higher energies above nTeV, Earth absorption increasingly suppresses upgoing neutrino events.

9.1 Background Rejection

Atmospheric air showers provide the dominant source of background events in the detector, with air-shower muons frequently having sufficiently high energies to penetrate the 1km ice overburden and reach the IceCube detector. However, this background only produces so-called downgoing events. Although the incident cosmic ray flux is roughly isotropic across the surface of the globe, horizontal and upward-going events are effectively suppressed by muon-shielding from the Earth. On the other hand, atmospheric air showers also produce a flux of atmospheric neutrinos, which is not shielded by the Earth. There is thus an isotropic atmospheric neutrino background, and an additional atmospheric muon background for southern declinations of the sky.

To reject the overwhelming muon background, southern-sky searches typically require strict energy cuts to reject atmospheric muons below approximately 10TeV. Above these energies, individual muons of atmospheric origin are unlikely. However, multiple daughter muons can

9.1 Background Rejection	35
9.2 Muon Track Reconstruction	36
LineFit	37
SPE	37
SplineMPE	37
SegmentedSplineMPE	37
Millipede	37
DNN/RNN	38
9.3 Topological Classification	38
9.4 Energy Reconstruction	38
MuEx	38
Truncated Energy	38
9.5 Pull Corrections	38
9.6 Event Selection	39
Cascade rejection	39
9.7 Systematic Errors	39
Ice Models	39
Detector Geometry	39
Atmospheric Flux Uncertainties	39
Pre-Pulses and After-Pulses	39
Jitter	39
DOM Efficiency	39
HiveSplitter + Coincidence	39
DOM Acceptance + Flasher Data	39
Spline Tables/Resolution etc.	39

travel as so-called muon bundles, which within the resolution of IceCube might appear to be one single high-energy muon. Often cascade-based southern-sky searches have superior sensitivity to muon-track based ones as a result of the improved energy resolution and suppressed muon-bundle background, as energy-based discrimination is the most effective separation method.

Northern-sky samples can typically probe lower-energies as a result of the reduced muon background, but upgoing fluxes with a large chord length through the Earth are suppressed. Consequently IceCube has peak sensitivity for horizontal events which benefit from both high background rejection and low earth absorption. It is in this region that track-like events at >200 TeV are typically found, including the high-energy neutrino event IC170922A which led to the identification of the first likely astrophysical neutrino source, TXS 0506+056.

For sufficiently high-energies, the low opacity to muons from air showers means that any atmospheric background event is very likely to be accompanied by additional and near-simultaneous muons from the same air shower. By rejecting so-called coincident events with multiple particles inside the detector, the so-called **self veto** becomes an effective method to reject southern-sky background at energies beyond nTeV. This significantly extends the air-shower rejection from the IceTop detector, which is only effective for near-vertical downgoing events.

One effective method to rejection background muons is to focus solely on so-called starting events, namely those for which the interaction vertex lies within the detector. Using outer detector layers as a veto reduces effective volume, but for such cases, almost all atmospheric muon backgrounds are rejected. Contained and partially-contained cascade events are similarly useful. Such a technique was employed to develop the High-Energy Starting Events (HESE) sample, with which the astrophysical neutrino flux was first discovered CITESCIENCE. A more flexible veto has been employed to enhance sensitivity to lower-energy neutrinos citeESTRES.

The muon and muon-bundle background is typically much more complicated to simulate realistically, since entire air-shower events are needed. As a consequence, while northern-sky samples have comprehensive Monte-Carlo-based background modelling, all-sky or southern-sky samples rely on data-based background models under the assumption that datasets are background-dominated.

9.2 Muon Track Reconstruction

Traditional IceCube reconstructions have relied of both algorithms and likelihood-based reconstructions. In the standard reconstruction chain, robust but simplistic algorithms are employed in order to generate a seed for likelihood-based reconstructions. The seeding approach ensures stability and speed.

LineFit

The LineFit Algorithm is the most simplistic approach to reconstructing a muon track, based on the assumption of a uniform cylinder of light traversing the detector at a constant speed. The arrival time of photons at each DOM is calculated, and the residual deviation from signal hypothesis is evaluated.

A χ^2 minimisation is then performed to match the model as closely as possible to observations. The result is a cylindrical pseudo-muon moving through the detector. Because of scattering and absorption, and the fact that the light is actually emitted in a conical shape, this direction only approximately follows that of the true muon direction. Nonetheless, it is extremely robust as a result of this simplicity, and thus forms the basis of most more-advanced reconstructions. An illustration of this algorithm is shown in Figure N.

WHAT PHOTON DATA? NO HIT INFO in data

SPE

One step beyond a χ^2 minimisation is to perform a full likelihood minimisation. In this case, if PDFs are constructed which accurately describe the physics in question, a more precise solution can be determined. The most simplistic model used in IceCube is the so-called **Single Photon Estimation** (SPE) likelihood. In this case, it is assumed that the first photon to arrive at a DOM is the one that is least scattered. This photon arrival time thus gives us the best indicator of the geometric distance the emitting muon.

A PDF is constructed, across all DOMs, comparing the arrival of this first DOM to those expected from photon propagation:

$$L = stuff$$

First photon is least scattered.

SplineMPE

Assumption continuous energy losses

SegmentedSplineMPE

Stochastic energy losses

Millipede

Cascades

Can fit with differing resolution

DNN/RNN

Azimuthal asymmetry in southern sky

Dust layer

9.3 Topological Classification

9.4 Energy Reconstruction

MuEx

Truncated Energy

9.5 Pull Corrections

In general, track reconstructions rely on reconstructing patterns of light emission from a muon traversing or exiting the detector. In that sense, they are more precisely muon track reconstruction algorithms. However, for the purposes of neutrino astronomy, we are instead interested in the neutrino direction.

For neutrino interactions, the direction of the outgoing daughter lepton is random in the center-of-mass frame. Viewed from the detector frame, the leptons are preferentially emitted in the direction of the incoming neutrino, with a spread depending on interaction opening angle. This **Kinematic Angle** between the neutrino and lepton is thus energy-dependent, with lower-energy neutrinos having on average larger opening angles. The Kinematic Angle θ_k can be approximately described as:

$$\theta_k \approx 1^{\text{deg}} \times \frac{E_\nu}{TeV}$$

Given the poor cascade resolution, the Kinematic Angle is thus primarily relevant for muon tracks where the muon energy is below 10TeV. This is however the parameter region in which the majority of the IceCube tracks fall, and is thus important to consider. The Kinematic Angle spread must be convoluted with the muon Point-Spread Function (PSF) in order to correctly model the expected distribution of tracks for a given neutrino source.

In an ideal case, this convolution would be done exactly. However, as discussed above, the neutrino energy for a given event can only be approximately determined. In practice, a correction must be performed based on the expected distribution of true neutrino energies corresponding to a given energy proxy value. Typically, this correction, known as a **Pull Correction** is performed using weighted Monte Carlo events under the assumption a particular true energy neutrino distribution. In IceCube, it is traditional to assume an E^{-2} spectrum.

In any case, this step introduces a fundamental energy-dependence to the neutrino PSF, which will unavoidably be present for any neutrino telescope in this energy regime.

9.6 Event Selection

Cascade rejection

9.7 Systematic Errors

Ice Models

One dominant source of systematic uncertainty in the IceCube detector is the ice itself, which is an inhomogeneous detector medium. Photon propagation is in

Detector Geometry

Atmospheric Flux Uncertainties

Pre-Pulses and After-Pulses

Jitter

DOM Efficiency

HiveSplitter + Coincidence

DOM Acceptance + Flasher Data

Spline Tables/Resolution etc.



10 Sources of astrophysical neutrinos

“...man will occasionally stumble over the truth, but usually manages to pick himself up, walk over or around it, and carry on.”

Winston Churchill, *Lady Windermere's Fan*, 18??

As far back as X, when nuclear fusion was proposed as a mechanism to power the sun, it was expected that a flux of solar neutrinos should be detectable on Earth. This prediction was confirmed by early neutrino detectors, ZZ and Z, which measured the flux xyc. The discovery of a source of neutrinos from beyond the solar system followed soon after, with the detection of nearby supernova SN1987A. Nearby supernova occur either within our galaxy, or in the neighbouring Magellanic clouds, at a rate of a couple per century. In the case of SN1987A, the detection of the supernova was preceded by simultaneous detections of an elevated neutrino flux in multiple detectors on Earth. The coincident detection of photons and neutrinos marked the first multi-messenger detection of an astrophysical source.

It is now well-understood that there is a diffuse flux of MeV-neutrinos produced from SN?, and preparations are underway for the inevitable next nearby SN, coordinated by the SuperNova Early Warning System (SNEWS). Given the increased volume of current-generation neutrino detectors, the next nearby supernova will be measured with much greater precision. IceCube itself will contribute to this, through a dedicated supernova detection system. Given the detector geometry, IceCube will not be able to identify individual neutrino events, nor reconstruct their directions. However, an increase in DOM noise will be clearly measurable, and likely with sufficiently resolution to resolve the time-evolution of the signal.

In both cases, the neutrinos detected at MeV-energies. However, in light of the discovery of a flux of high-energy astrophysical neutrinos by IceCube, a new branch of astronomy has developed searching for

10.1 Galactic Neutrino Emission	43
10.2 Emission from the Local Universe	44
10.3 Blazars	44
TXS 0506+056	45
10.4 Gamma-Ray Bursts	46
10.5 Core-Collapse Supernova	47
10.6 Tidal Disruption Events (TDEs)	48
10.7 Fast Radio Bursts	50
10.8 Active Galactic Nuclei and Starburst Galaxies	50

sources of these astrophysical neutrinos. The central fact for neutrino astronomy, at least in the TeV-PeV range for which IceCube is sensitive, is that at lower energies there is an overwhelming background, while at higher energies, statistics are poor. This is illustrated in Fig. The power of IceCube to detect an astrophysical flux depends on the degree to which this differs from the atmospheric background. Above all, the expected energy distribution for most astrophysical sources likely differs from the soft-spectrum atmospheric neutrino flux. In addition, the spatial distribution of the background is broadly isotropic, and uniform as a function of right ascension. The temporal distribution of this background, beyond small-scale season variations, is also reasonably isotropic. Foreground fluxes which differ substantially will be most easily detected.

The expected degree of anisotropy in the extragalactic astrophysical neutrino flux strongly depends on the properties of the assumed sources, in particular their density and source evolution. The source evolution describes the rate or density evolution of astrophysical objects as a function of redshift. For sources with a negative source evolution, the density in the local universe is greater than at high redshift, so there are fewer neutrinos produced by distant, unresolved sources. Conversely, for a strongly positive source evolution, we expect a greater fraction of neutrinos to arrive from unresolved sources. When local density and source evolution are coupled, we then find arrive at a flux which is anisotropic to varying degrees. Given that the atmospheric backgrounds are broadly isotropic, and uniform as a function of right ascension, the sensitivity of IceCube to a given astrophysical flux will depend strongly on whether that flux is sufficiently spatially anisotropic to distinguish it from atmospheric backgrounds. A higher-density source population, with positive evolution, would be much harder to identify than a low-density one with negative evolution. Anisotropy in neutrino arrival times can be an additional metric to distinguish astrophysical neutrinos. For sources which are variable or transient, neutrino emission is only expected for distinct time periods, eliminating background events.

In general, given knowledge about the background, the most agnostic methods to identify neutrino sources look for clustering within the data without reference to external datasets. Such auto-correlation analyses can be done with either a time-integrated or time-dependent all-sky likelihood scan. The result of such an analysis is a pixelised likelihood map. Comparisons of this map can then be made to expectations from background, either using the single "hottest spot" in the sky, or by comparing the distribution of hotspots. No significant excess was found for either approach, providing significant general constraints on neutrino source populations. Given the current detector volumes and resolution, as well as the lack of observed lower-significance overfluctuations, it appears that the astrophysical neutrino flux is not sufficiently anisotropic for auto-correlation analyses to discover a neutrino source in the near future.

As an alternative to agnostic searches, specific source hypothesis tests can be substantially more sensitive. Given the position of a known

astrophysical object, the threshold for a significant excess is greatly reduced due to the avoidance of an all-sky trial factor. Sensitivity can be further enhanced when information from multiple objects is combined in a so-called ‘stacking search’. These methods can be used to test for neutrino excesses correlated to astrophysical populations. One drawback of these methods is that their sensitivity strongly depends on the quality of available multi-wavelength data. Often these catalogues are not complete, particularly in the case of transient or variable objects.

On the other hand, realtime analysis is a complementary method that inverts this traditional object neutrino relationship. Instead of taking a known object, and asking whether neutrinos are correlated to it, realtime analysis identifies likely-astrophysical neutrinos and seeks to identify coincident astrophysical objects that could potentially have produced the neutrino. The power of realtime searches is that they can, if a possible counterpart is identified, lead to contemporaneous multi-wavelength follow-up that maybe reveal more about a given object. Within this context, the

However, it should be noted that both realtime and stacking analyses are only sensitive to cases where neutrino sources have detectable EM counterparts. It might however be the case that EM emission from neutrino sources is either absorbed or attenuated, and consequently stacking analyses will be unable to identify such EM-dark neutrino sources. Furthermore, particularly for CCSNe-like populations following the Star Formation Rate (SFR), a large fraction of the astrophysical neutrino might in fact come from unresolved sources.

10.1 Galactic Neutrino Emission

As can be seen in Fig, the galactic plane accounts for a significant fraction of EM emission in every wavelength, from radio to high-energy gamma rays. It is therefore natural to suspect that the Milky Way might contribute to the astrophysical neutrino flux. Likely sources of galactic neutrinos are much the same as high-energy gamma rays, namely Supernova Remnants (SNRs) and Pulsar Wind Nebulae (PWNe). In addition, given that the galaxy should act as a target for extragalactic UHECRs and thus produce secondary neutrinos, it is guaranteed that some galactic contribution should be present in the neutrino flux. Despite this expectation, to date no significant galactic neutrino excess has been found. Given the position of the galactic center in the southern hemisphere, where IceCube muon track datasets are less sensitive, IceCube searches are typically conducted using likely-astrophysical cascades. These searches have in some cases been conducted jointly with the northern-hemisphere ANTARES neutrino observatory, and additionally with HAWC high-energy gamma-ray detector. At this point, limits on the galactic neutrino flux are beginning to constrain reasonable models, above all the standard KRA- γ model. Given constraints limiting the galactic contribution to less than n% of the diffuse flux, we can state with certainty that the astrophysical neutrino flux must be **predominantly extra-galactic**.

Specific tests were performed on likely galactic sources of high-energy neutrinos, but none have identified any specific excess. The latest constraints limit the contributions of PWNe and SNRs to be less than Y% and Z% respectively.

An additional analysis was performed on the Fermi Bubbles, a large gamma-ray-emitting region perpendicular to the galactic plane. The origin of the Fermi Bubbles is still unclear, but one explanation is X. Neutrino emission might be expected from XYZ, however no excess was found.

Fermi Bubbles

10.2 Emission from the Local Universe

As with the galactic plane, it is expected that collisions between UHE-CRs and matter in the local universe should produce a secondary flux of high-energy neutrinos, regardless of the ultimate origin of the UHE-CRs. Additionally, the primary flux of astrophysical neutrinos might well be correlated with the local matter density of the universe, for example in cases where neutrinos are produced from X, Y or Z. Both cases were tested through a correlation analysis between neutrinos and local matter density as defined by the 2-mm Redshift Survey (2MRS) catalog. 2MRS survey and stuffs.

10.3 Blazars

One long-favoured candidate neutrino source class is Blazars, the sub-class of Active Galactic Nucleii (AGN) with relativistic particle jets that point towards the Earth. These blazars have long been known to emit both high-energy and Very-High Energy (VHE) gamma-rays in the MeV-TeV range. Extensive modeling of these objects, particularly nearby examples such as BL-Lac and Markarian 421 (Mrk 421), have revealed a characteristic SED with two characteristic "humps", as shown in Figure n. While there is consensus that the lower-energy hump likely arises from synchrotron emission, the higher-energy one has been explained both by leptonic and hadronic models. Neutrino emission would be expected for the latter in all cases, but never the former.

Since 200n, there have been extensive observations by the Fermi Large Area Telescope (Fermi-LAT), an MeV-GeV gamma-ray satellite telescope. With a significantly increased sensitivity over its predecessors, Fermi has discovered n00 blazars as of 4FGL, adding to the n from previous mission.

It is now known that blazar emission dominates the high-energy gamma-ray sky. Modelling of the "Extragalactic Background Light" (EBL) typically assumes that 80% of all gamma-ray emission in the Fermi range is produced by blazars. IACTs have also confirmed that blazars such as Mrk 421 are extremely bright at TeV gamma-rays.

Although photons at these energies are quickly attenuated during propagation due to interactions with CMB PHOTONS, it is assumed by extrapolation from observations of nearby blazars that more distant ones are also likely TeV-emitters.

Given the simultaneous production of gamma-rays with neutrinos in hadronic interactions, it is natural to suspect that bright gamma-ray sources, namely blazars, may additionally be neutrino sources. This hypothesis has been tested repeatedly by IceCube, and under the assumption of a linear proportionality, the contribution of all blazars has been constrained to less than 6% of the astrophysical neutrino flux. This limit additionally accounts for the contribution of unresolved blazars, as well as those in the 3FGL? catalogue that were tested. A more agnostic search on 3FHL blazars constrained their contribution to be less than 20-30%, without limiting the contribution of unresolved blazars. In both cases, it must be pointed out that this limit is dependent on assumed spectral index. These constraints generally disfavoured blazars as neutrino sources, with fine-tuned models required to generate neutrinos from lower-luminosity unresolved blazars without violating constraints on the brighter resolved blazars.

TXS 0506+056

However, this interpretation was challenged by the observation of IC170922A, a high-energy neutrino that arrived in spatial and temporal coincidence with a bright gamma-ray flare from blazar TXS 0506+056. A likelihood analysis correlating high-energy neutrinos with the monthly gamma-ray lightcurves of Fermi blazars led to the disfavouring of a chance coincidence at the level of 3σ . This result implied that, rather than the average gamma-ray flux, high-energy neutrinos might instead be correlated with instantaneous gamma-ray flux. Prompted by this observation, the IceCube collaboration conducted a time-dependent search for archival neutrino emission from the direction of TXS 0506+056, and identified a signal-like neutrino cluster in 2014-15 with a significance of 3.5σ . Surprisingly, this neutrino cluster was not accompanied by any significant contemporaneous gamma-ray activity CITESIM. TXS 0506+056 thus presented a somewhat contradictory picture, with both pieces of evidence challenging to interpret in a unified framework. Theoretical attempts to model the arrival of IC170922A were generally successful, particularly when accounting for the likely Eddington Bias in any flux estimation. However, attempts to model the arrival of the neutrino cluster were significantly more challenging as the implied neutrino flux was much greater than the measured gamma-ray flux. Despite relatively poor observational constraints for the 2014-15 period, there have been no successful models describing all claimed neutrino emission from TXS 0506+056.

In general, how to resolve the apparent incoherence of these observations remains an open question. Additionally, it remains unclear whether or how TXS 0506+056 is, in some way, "special". If it were simply one of many neutrino blazars emitting proportionally to its gamma-ray flux, we would have expected the stacking analysis to

identify a correlation with higher significance. On the other hand, if the source is in some way unique, then the observed behaviour would be more coherently understandable. One study promptly identified that the hitherto-accepted classification of TXS 0506+056 as a BL-Lac was incorrect, and it was in fact an FSRQ. As a member of the rare subclass of ‘masquerading BL-Lacs’, it had a specific properties which in some models would indicate enhanced neutrino emission. There has been some recent evidence that TXS 0506+056 has a unique jet geometry, citeBRITZEN, but there is to date there is no model which has attempted to connect this geometry to observations of neutrino emission. A search for additional neutrino clusters from blazars in 4FGL did not reveal any significant excess correlation with either FSRQs or BL-LACs.

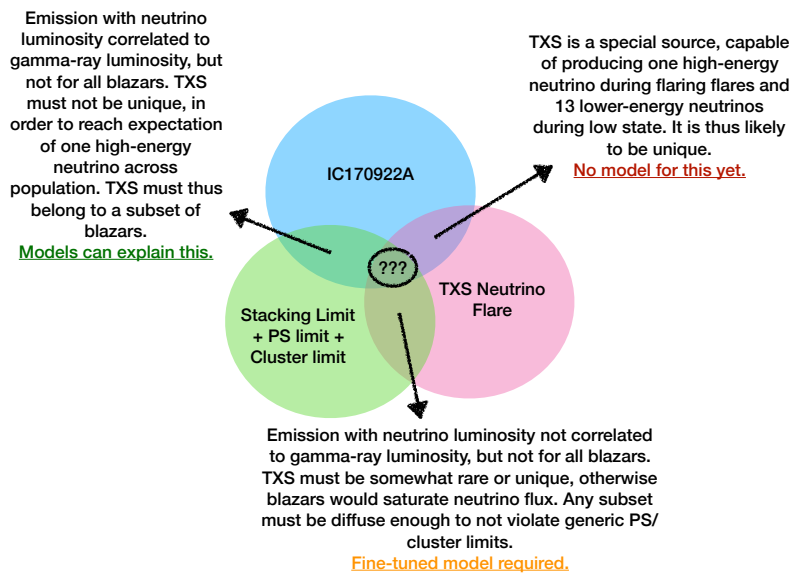


Figure 10.1: The challenge of coherently understanding the scenarios for neutrino emission from blazars, given the two pieces of evidence from TXS 0506+056, as well as the constraints from IceCube stacking analyses, general point-source searches and generic time-dependent cluster searches. To date, no model has resolved all three observations coherently.

10.4 Gamma-Ray Bursts

Gamma-ray Bursts (GRBs) have long been proposed as a source of neutrinos. GRBs themselves fall into two broad categories, short and long, which are believed to arise from distinct physical populations. Long GRBs have been associated with the appearance of broad-lined type Ic supernova, and are thus believed to arise from a relativistic jet produced during supernova explosion.

Short GRBs are now known to arise from relativistic jets launched during the merger of binary neutron stars. The first, and to date only, observed coincidence occurred for the gravitational wave event GW170817, which was associated with the short GRB 170817A and the kilonova AT2017gfo. Observations of GRB170817A revealed that it was particularly underluminous relative to most short GRBs, a fact later explained by comprehensive observations and modelling of AT2017gfo that confirmed an off-axis jet geometry. Given the relatively narrow jet opening angle, it is expected that the majority of future binary

neutron star mergers detected by LIGO will not have detectable GRB counterparts.

Afterglow for both?

For both short and long GRBs, neutrino emission might be expected during the so-called "prompt phase" of gamma-ray emission. IceCube has undertaken numerous searches for neutrino emission, but has so far observed no correlation. Prompt emission from GRBs is particularly favourable for neutrino detection, because the brief and well-defined search period greatly reduces the expected background for such searches. This scenario is indeed one of the most-constrained by IceCube, which current limits restrict to less than 1% of the astrophysical neutrino flux.

Our understanding of GRBs has recently expanded further after the discovery of GRB VHE gamma-ray emission by MAGIC and HESS collaborations. The timescales for this emission, extending as much as 18 days after prompt phase indicates that high-energy processes extend throughout the so-called afterglow phase. consequently there is renewed focus on potential neutrino afterglow emission, which is significantly less-constrained. One previous Icecube analysis limited the contribution to n% (cite HESE).

An additional subclass are so-called low-luminosity GRBs (LLGRBs), believed to be... Given the poor efficiency with which source sources are detected, stacking searches of LLGRBs are significantly less powerful. However, for this case, generic searches for short-scale neutrino multiplets provide constraints on the contribution of such a population. In this case, they are known to contribute less than x%.

10.5 Core-Collapse Supernova

Supernovae, the explosive death of stars, are perhaps the best-studied phenomenon in astronomy. They are traditionally classified based on observed properties, rather than intrinsic physical attributes. An overview of a classification scheme is given in Figure ???. The most fundamental distinction is in explosion mechanism, with Type 1a SNe occurring due to thermonuclear explosions while all other classes are believed to arise from stellar core collapse. Further distinctions are made based on emission line, yielding the classes of Type Ib, Ic and Type II. Some SNe are observed to have narrow lines, which occur due to interaction with ejecta and circumstellar material (CSM). These supernova are denoted with 'n', the most common being Type IIn. This group in particular are candidate neutrino sources, in which neutrinos are produced via CSM interactions. An additional class of SNe is the IIP subclass, the subset of Type II SNe for which a characteristic lightcurve plateau is observed. Such plateaus are typically assumed to arise from.... Those Type II supernova not falling into IIP are instead classified as IIL, with characteristic Linear decay lighcurves.

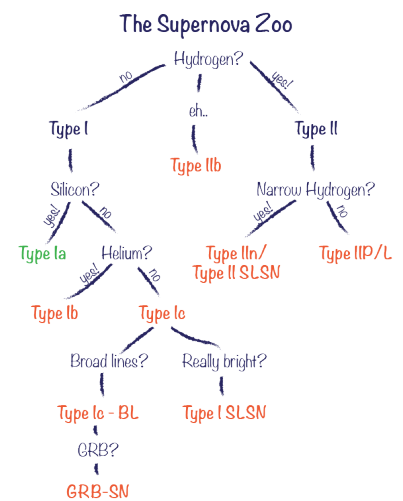


Figure 10.2: An overview of the current supernova classification scheme, which has been recently expanded to include superluminous supernova. Type 1a supernovae, marked in green, arise from thermonuclear explosions. All other classes, marked in orange, occur due to core collapse.

Type Ic SNe can occasionally be observed with spectroscopic features known as Broad-Lines, which typically indicate the presence of fast-moving material. These form a distinct subclass, and it is this subclass which has been associated with long GRBs. Though radio observations have excluded the possibility that all Ic-BL SNe host relativistic jets? it is expected that even those without an observed GRB may instead host so-called 'choked jets'. These occur if a relativistic jet is launched during core collapse, but because it lacks sufficient power to break through the outer layers of stellar material, it is stopped within the interior of the star. These choked jets, much like their standard counterparts, could produce neutrino emission. This scenario is however particularly difficult to test, because only those choked jets aligned towards Earth would produce a neutrino signal. As the alignment of a choked jet cannot be measured, it is impossible for us to say which supernova should or should not produce neutrinos.

An additional category of supernovae has been recently observed, identifiable by their atypical brightness. So-called Superluminous supernovae (SLSNe) were initially classified as any SNe with an absolute magnitude brighter than -21 mag. However, in recent years, increased study has led to a spectroscopic classification being favoured, with some dimmer objects in the range $-20 < M < -21$ also being accepted. There are currently two favoured models to explain why SLSNe are so bright, namely the Magnetar model and the PISN model.

10.6 Tidal Disruption Events (TDEs)

Roche Limit== The tidal radius can best be understood by comparison to the more straightforward concept of the Roche Limit, otherwise known as the Roche Radius. The Roche Radius is defined as the distance at which the self-gravitational force acting on the outer surface of a body are exactly equal to the gravitational pull of a second body on that same mass element. If a star moves closer than its Roche Radius for an SMBH, there will be a net force on mass elements on the star surface towards the SMBH, and the star will disintegrate.

The Tidal Force of one body acting on another is simply the difference in gravitational force strength between the closer surface of the sphere and its core. The Tidal Force of a black hole of mass M and distance d , acting on a mass element u lying on the closest point of the stellar surface, is thus given by:

$$F_{tidal} = \frac{GMu}{(d-r)^2} - \frac{GMu}{(d)^2}$$

$$F_{tidal} = \frac{GMu}{d^2} \left((1 - \frac{r}{d})^{-2} - 1 \right)$$

Using Binomial Expansion with the reasonable assumption that $r \ll d$, we reach an approximation:

$F_{tidal} \approx \frac{GMu}{d^2} \times \frac{2r}{d}$ The Roche Radius for a black hole of mass M for a star of mass m and radius r is thus found by equating this with the self-gravitational force acting on the same mass element.

$$F_{grav} = \frac{Gmu}{r^2} = \frac{2Gmur}{d^3} \approx F_{tidal}$$

$$d = r \times \left(\frac{2M}{m}\right)^{\frac{1}{3}} \approx r_{roche}$$

== Tidal Radius ==

This simplistic model does not hold for Tidal Disruption Events. The tidally-disrupted body would need to be in a circular orbit with synchronised spin, but stars tend to have approach Black Holes parabolically. In addition to Angular Momentum, General Relativity should be accounted for. This is particularly relevant for large black holes. A rigorous definition of Tidal radius should account for these things, but in any case, the point at which a star becomes ‘tidally disrupted’ is difficult to define. An event which only strips a fraction of the outer shell of the star would be ambiguous. Fortunately these definitions differ only by the order of unity from the Roche Radius. In the original paper introducing these calculations by [<https://www.nature.com/nature/journal/v333/n6173/abs/333523a0.html> Rees (1988)], the tidal radius was defined as the radius at which the mean internal density of the star is exceed by the mean internal density of the orbital volume. In this definition:

$$\rho_{star} = \frac{m}{\frac{4}{3}\pi r^3} = \frac{M}{\frac{4}{3}\pi d^3} = \rho_{volume}$$

$$d = r \times \left(\frac{M}{m}\right)^{\frac{1}{3}} = r_{tidal}$$

Thus we see that:

$$r_{tidal} = \frac{r_{roche}}{\sqrt[3]{2}}$$

In any definition of a characteristic tidal radius, we nonetheless always find that the radius scales with the cubic root of mass. It is interesting to recall that, in contrast, the Schwarzschild Radius of a black hole scales linearly with its mass.

$$R_S = \frac{2GM}{c^2}$$

Consequently, the Schwarzschild Radius of the Black Hole grows faster as a function of Mass than the tidal radius. There is thus a critical black hole mass, for which the Schwarzschild Radius equals the star’s Tidal Radius. Above this, a TDE cannot occur, because the star would have to be wholly swallowed by the black hole in order to be tidally disrupted. Though the exact limit will vary somewhat depending on the mass of the star, using typical values gives us an order-of-magnitude upper limit on TDE-generating black holes of $M < 10^8 M_\odot$.

== Post-Disruption Evolution ==

For TDEs, the accretion of stellar material produces a highly-luminous flare, which is often the cause of discovery. This can be visible in Optical, UV or Xrays. The bound mass spirals into the Black hole, but the fall-in time of each mass element in the bound material depends on the Gravitational Potential Energy of the element, leading to a characteristic fall-in rate $\frac{dM}{dt} \propto t^{\frac{5}{3}}$ relation. This, in turn, can be seen in the light curves of TDEs.

There is evidence to support the existence of jetted TDEs, and these are usually highly-luminous in X rays. However, the classification of candidates into jetted or non-jetted can be unclear.

There is a further proposed model in which an envelope forms around the Black Hole, which could lead to choked jets.

== Neutrino Emission ==

The process for neutrino emission in TDEs, as well as the expected rates and neutrino light curves, are all highly uncertain. A key component of this analysis will be to probe the importance of an accurate time PDF, and the degree to which a minimal-assumption wide box model is the optimal time PDF to use. Even assuming the shape of the expected light curve was well known for each TDE (either the same neutrino light curve for every TDE, or one closely correlated to the TDE optical or X Ray light curve), there remains a significant degree of uncertainty regarding the delay between neutrino emission and optical emission. It is possible that the peak neutrino emission is achieved more than 100 days before optical peak, but the expected gap is entirely model-dependent. The following potential models have been proposed for Neutrino Acceleration:

* Jetted TDEs, such as Swift J1644-57 * Choked Jet Scenario

Tidal Disruption Events (TDEs) are rare transients that occur when stars pass close to supermassive black holes (SMBHs). Studies have suggested that TDEs are sources of high-energy neutrinos and ultra-high energy cosmic rays[[2009ApJ...693..329F](#), [2017MNRAS.469.1354D](#)], in particular those TDEs with relativistic particle jets[[2014arXiv1411.0704F](#), [2017ApJ...838....3S](#), [2016PhRvD..93h3005W](#), [2017PhRvD..95l3001L](#)]. TDEs with non-thermal radio emission are considered the most likely candidates for sources of high-energy neutrinos.

10.7 Fast Radio Bursts

A relatively recent astro

10.8 Active Galactic Nuclei and Starburst Galaxies

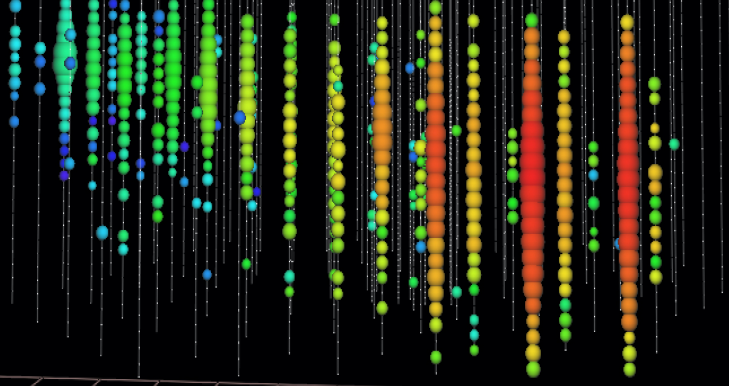
One additional possibility is that the astrophysical neutrino flux is produced by a large population of steady sources, and is thus truly a **diffuse** astrophysical neutrino flux. One case would be for neutrino production in Starburst Galaxies, which has been suggested in various models x.

Starburst galaxies are those galaxies for which there is a high level of star formation. Such galaxies have elevated supernovae rates, and are typically bright in UV and such. Starburst galaxies have been detected in gamma rays, including at very high energies, confirming the existence of acceleration processes. A search for neutrino emission from Starburst Galaxies was performed in x, and no significant correlation was identified. Given the expected dominant contribution from unresolved Starburst galaxies to any population neutrino flux,

and accounting for the fact that this aggregate flux must not exceed the measured astrophysical neutrino flux, it is clear that the nearby starburst galaxies must therefore be very weak neutrino emitters. Such a scenario is unfavourable for identification against an isotropic neutrino background, and in this case it is unlikely that IceCube would have sufficient sensitivity to identify the neutrino flux origin.

A similar case would occur in that case of neutrino production from the cores of Active Galactic Nuclei (AGN), as suggested by XYZ. Here neutrinos would arise from pn interaction occurring in the inner accretion disk of AGN, with the corresponding gamma-ray emission being absorbed. Such a scenario is appealing theoretically, as it would neatly evade the existing constraints on diffuse gamma-ray emission, which we know to arise predominantly from blazars. This hypothesis was tested by IceCube (I hope...)

SUMMARY TABLE with source class, limit, and spectral index



11 Realtime Multi-Messenger Astronomy

In recent years, there has been a significant renewed interest in the study of transient and variable objects in astronomy. Driven primarily by the speed at which objects can evolve and disappear, particularly GRBs and latterly Kilonovae, it is often essential that astronomy can be done with minimal latency. In this vein, it is now commonplace for detectors to automatically issue so-called alerts for observations that meet given criteria, to enable other instruments to rapidly obtain near-simultaneous observations. Realtime alerts are automatically issued by GRB-searching instruments such as Swift-BAT and Fermi-GBM, while gravitational-wave events are issued by the LIGO-VIRGO observatories, and high-energy neutrino alerts are issued by IceCube as well as ANTARES.

These alerts are all typically issued via the Gamma-ray Coordination Network (GCN) system, where observatories can subscribe to automatically be notified or point. An essential component of this process is the additional information published by astronomers, via GCN or Astronomers Telegrams (ATELs), in which follow-up observations are coordinated. There have been two high-profile examples of this, namely the comprehensive followup of GW170817/GRB170817A that led to the first unambiguous observation of a kilonovae, and the followup of high-energy neutrino IC170922A, which led to the identification of TXS 0506+056 as the first candidate source of TeV neutrinos.

As part of this thesis, the author maintained and further developed the IceCube Realtime System from October 2018 onwards, acting as first responder to the vast majority of neutrino alerts in that period.

11.1 The IceCube Realtime System

The IceCube Realtime System has been operating since 2016, providing the first source of high-energy neutrino alerts. The first iteration of the alert system consisted of two streams, namely High-Energy Starting Events (HESE) and Extremely High Energy (EHE) events CITE. Each

11.1 The IceCube Realtime System	53
IC160427A - The "PanSTARRS Supernova Neutrino"	54
IC170922A The "TXS 0506+056 Neutrino"	55
IC190331A - The "Multi-PEV Neutrino"	55
IC190730A - The "PKS 1502+106 Neutrino"	55
IC190922B - The "SN2019pqh Neutrino"	56
IC191001A - The "Bran Stark Neutrino"	56
IC200107A - The "Flaring Extreme Blazar neutrino"	56
11.2 Interpreting high-energy neutrino alerts	56
Cluster searches	56
OFU and GFU	56

was an established event selection used to identify likely-astrophysical neutrinos cite. Filters to identify relevant events are deployed on computers at the South Pole, and detections are flagged with low latency. After fast "online" reconstruction algorithms are applied to events, an automated machine-readable "notice" is distributed via the GCN system. In parallel, data from the event is transmitted via satellite to a computing centre in Madison, Wisconsin where a full likelihood scan is performed on the event (see chapter ?? for more details).

Give V1 rates!

The alerts are vetted by humans to asses the event quality, with visually inspection being used to confirm classified topology and event reconstructions. The operating state of the detector is additionally checked. Following these steps, a plain-text GCN circular is distributed via the GCN system to confirm the good nature of the alert, and to provide the updated localisation arising from the full scan.

This original system of alerts continued until May 2019, at which point a new alert system was implemented. While the original EHE selection was maintained, the HESE alert selection was improved to reduce the cascade contamination, and improve the astrophysical purity. In addition, a new alert stream based on the GFU event selection was initiated, with a significantly-elevated rate relative to EHE and HESE alerts. The publication of these three alert streams was unified into a new IceCube Astrotrack GCN stream, which was further subdivided into Gold and Bronze based on the average purity of alerts. Golden Astrotrack alerts will, as an ensemble, have an average of 50% astrophysical neutrinos, while Bronze Astrotrack will have an average of 30% astrophysical neutrinos.

A summary of all neutrino alerts issued to date is provided in table X. Individual neutrino alerts of interest are summarised in subsequent sections.

IC160427A - The "PanSTARRS Supernova Neutrino"

The first alert issued under this system, HESE alert IC160427A, was found to be in spatial coincidence with an optical transient detected by the Pan-STARRS Observatory while following up the alert. This transient was initially tentatively classified as a Type Ic supernova, for which various models have predicted neutrino emission (see Chapter 10). However, the further spectroscopic and photometric evolution indicated that this was more likely a Type Ia Supernova, for which no neutrino emission would be expected. Nonetheless, dedicated efforts to simulate an ensemble of IC160427A-like events led to the first characterisation of the impact of systematic uncertainties in modelling the polar glacial ice on directional reconstruction with IceCube for high-energy alerts.

IC170922A The "TXS 0506+056 Neutrino"

Subsequent neutrino alerts did not yield any probable counterparts, until the detection of EHE alert IC170922A in spatial coincidence with flaring blazar TXS 0506+056. Chance coincidence in this case was estimated. This event was also resimulated in the same manner as IC160427A. Remarkably, despite its radically-different topology of through-going muon rather than starting track, the results were found to be broadly consistent. More details are given in chapter N.

IC190331A - The "Multi-PEV Neutrino"

A starting track was observed

IC190730A - The "PKS 1502+106 Neutrino"

IC190730A was a golden neutrino alert with a signalness of roughly 65%. Following the automated notice, Millipede Reconstruction clearly showed it was well-localised, and spatially coincident with blazar PKS 1502+106. This particular blazar is extremely bright, being Nth brightest in the sky in terms of integrated gamma-ray energy flux, and owing to its high redshift of $z=1.000$, is one of the most luminous known blazars. This coincidence was reported in the corresponding GCN circular, and triggered a broad multi-wavelength follow-up campaign. The archival SED is provided in figure N, originally from X, but annotated to illustrate contemporaneous observations from other instruments.

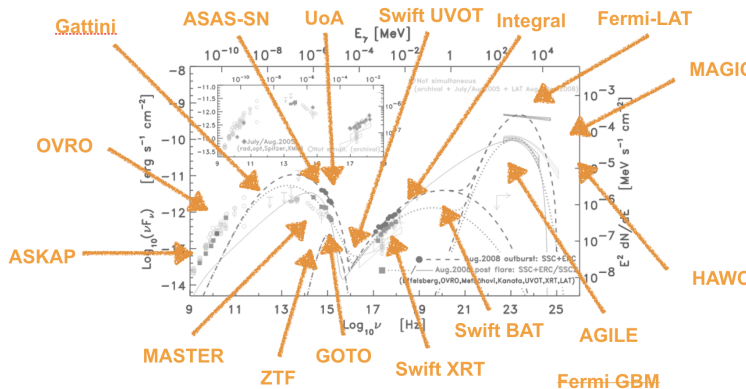


Figure 11.1: The archival SED of PKS 1502+106 from X is shown. In orange, the names of various instruments that observed the source are shown, with orange arrows to indicate their corresponding energy regimes. CITEA-Z

Despite comprehensive wavelength coverage,

The chance coincidence for at least one neutrino alert to be coincident with any of the 15 brightest blazars was calculated by the author, and found to be disfavoured at the level of 2.0 sigma following the procedure in N.

IC190922B - The "SN2019pqh Neutrino"

IC191001A - The "Bran Stark Neutrino"

IC200107A - The "Flaring Extreme Blazar neutrino"

11.2 Interpreting high-energy neutrino alerts

lalala

Cluster searches

lalaland

OFU and GFU



12 Transient Follow-up with ZTF

// ...lalala.

//

Winston Churchill, *Lady Windermere's Fan*, 18??

The motivation for all real-time analysis and prompt follow-up observations of external triggers is to obtain contemporaneous data. Put another way, these observations are designed to quickly identify time-dependent transient or variable activity which would be missed by untargeted survey operations. In the case of GW and short GRB follow-up, searches are targeted towards identifying kilonovae (KNe), of which GW170817/AT2017gfo was a spectacular well-documented first example. These KNe are inherently fast-evolving transients which will by definition not be present before the extrenal trigger. For neutrinos, there are a proliferation of possible optical transients (e.g GRBs, TDEs, SNe) and variable objects (primarily blazars) which could be identified in an optical follow-up observations. In both cases, a handful of potentially interesting extragalactic objects will need to be selected against a vast background of spurious detections, and unrelated galactic or solar-system objects.

12.1 The AMPEL Follow-up Pipeline	57
12.2 Neutrino Follow-up	58
PKS 1502+106	60
SN2019pqh	60
12.3 Gravitational Waves and Gamma-ray Bursts	61

12.1 The AMPEL Follow-up Pipeline

Given the similar challenge, a single flexible analysis, the *AMPEL Follow-up Pipeline*, was developed by the author to identify candidate counterparts to GW, GRB and neutrino trigger events. ZTF is particularly well-suited to this type of extragalactic transient discovery, because ZTF routinely images the visible Northern Sky once every three nights to a median depth of 20.5^m as part of a public survey

[2019PASP..131g8001G, 2019PASP..131a8002B]. This provides an extensive base to distinguish between new transients that could be coincident with an external trigger, and those with previous detections. The large volumetric survey speed of ZTF often provides significant serendipitous coverage of events. This wide-field cadence can however be supplemented by dedicated Target-of-Opportunity (ToO) observations scheduled for a particular trigger through the GROWTH ToO Marshal [2019PASP..131d8001C].

Following both survey and ToO observations, the raw images are processed by IPAC, and alert packets are promptly generated for significant differences relative to survey reference images [2019PASP..131a8003M, 2019PASP..131a8001P]. These alerts are then distributed as part of a near-realtime stream to brokers, and are archived in a database of alert packets at DESY as part of the local infrastructure for multi-messenger data analysis (the *archive database*).

External triggers, which come in the form of probability skymaps or GCN circulars, are downloaded and parsed with *AMPEL Follow-up Pipeline*. The archive database is then queried for coincident alerts, using either temporal indexing or spatial indexing depending on the size of the target region. Once loaded, these alerts are then filtered by the *AMPEL Follow-up Pipeline* using AMPEL [2019A&A...631A.147N], a platform for realtime analysis of multi-messenger astronomy data. Our selection is based on an algorithm for identifying extragalactic transients [2019A&A...631A.147N]. In order to identify candidate counterparts, we apply the following cuts to ToO and survey data:

- ▶ We reject likely subtraction artifacts using machine learning classification and morphology cuts [2019PASP..131c8002M]. Subtractions must be positive, i.e a candidate must be brighter than the same position in stacked reference images.
- ▶ We reject solar system objects through matches to known catalogues [2019PASP..131a8003M]. We further remove uncatalogued solar system objects by requiring multiple detections for each candidate at the same location, separated temporally by at least 15 minutes, thereby rejecting moving objects.
- ▶ We reject galactic stellar sources by removing detections cross-matched to objects with measured parallax in the second data release of the GAIA satellite [2018A&A...616A...1G]. Objects are rejected if they have non-zero parallax with a significance of at least 3σ . We further reject likely stars with machine learning classifications, based on sources detected by Pan-STARRS1 [2018PASP..130l8001T], removing those objects with an estimated stellar probability greater than 80%.
- ▶ We reject AGN variability by cross-matching objects to the WISE survey. We identify likely AGN by applying a series of cuts based on measured IR colour [2010AJ....140.1868W].
- ▶ We rejected unassociated objects by requiring both spatial and temporal coincidence with a given trigger.

[2019A&A...631A.147N]:
2019A&A...631A.147N
(2019A&A...631A.147N),
2019A&A...631A.147N

[2019PASP..131c8002M]:
2019PASP..131c8002M
(2019PASP..131c8002M),
2019PASP..131c8002M

[2018A&A...616A...1G]:
2018A&A...616A...1G
(2018A&A...616A...1G),
2018A&A...616A...1G

[2018PASP..130l8001T]:
2018PASP..130l8001T
(2018PASP..130l8001T),
2018PASP..130l8001T

[2010AJ....140.1868W]:
2010AJ....140.1868W
(2010AJ....140.1868W),
2010AJ....140.1868W

Table 12.1: Summary of the eight neutrino alerts followed up by ZTF, with IC191001A highlighted in bold. The 90% area column indicates the region of sky observed at least twice by ZTF, within the reported 90% localisation, and accounting for chip gaps. The *signalness* describes the probability that each neutrino is of astrophysical origin, rather than arising from atmospheric backgrounds. One alert, IC200107A, was reported without a signalness estimate.

Event	R.A. (J2000) (deg)	Dec (J2000) (deg)	90% area (sq. deg.)	ZTF obs (sq. deg.)	Signalness	Ref
IC190503A	120.28	+6.35	1.94	1.37	36%	[blaufuss:gcn24378, 2019ATel13160]
IC190619A	343.26	+10.73	27.16	21.57	55%	[blaufuss:gcn24910, 2019ATel13160]
IC190730A	225.79	+10.47	5.41	4.52	67%	[stein:gcn25225, 2019ATel13160]
IC190922B	5.76	-1.57	4.48	4.09	51%	[blaufuss:gcn25806, 2019ATel13125]
IC191001A	314.08	+12.94	25.53	20.56	59%	[stein:gcn25913, 2019ATel13160.....]
IC200107A	148.18	+35.46	7.62	6.22	-	[stein:gcn26655, stein:gcn26802]
IC200109A	164.49	+11.87	22.52	20.06	77%	[stein:gcn26696, reusch:gcn26802]
IC200117A	116.24	+29.14	2.86	2.66	38%	[lagunas:gcn26802, reusch:gcn26802]

12.2 Neutrino Follow-up

ZTF has since its inception had a dedicated program to identify sources of high-energy astrophysical neutrinos, through targeted follow-up observations. Given the proliferation of proposed source classes, neutrino follow-up are characterised by searching relatively well-localised regions for poorly-defined objects. This is particularly true for optical follow-up, where potential counterparts include Tidal Disruption Events (TDEs), Type IIn or choked jet SNe, kilonovae, GRB afterglows, superluminous supernovae (SLSNe) or blazar flares. While pre-neutrino detections could rule out neutrino production from choked jet supernovae, in most cases we do not even have stringent constraints in when neutrinos may be expected

We have followed up eight neutrinos in the period from survey start on 2018 March 20 to 2020 March 31, out of a total of 31 neutrino alerts published by IceCube. Table 12.1 summarises each neutrino alert that has been observed by ZTF. From 2019 June 17, IceCube published neutrino alerts with improved selection criteria to provide an elevated alert rate [2019ICRC...36.1021B] (see Chapter 11 for more details). In addition to 1 of the 12 alerts under the old V1 selection, ZTF followed up 7 of the 19 alerts published under the V2 selection. In general, we aim to follow all well-localised neutrinos of likely astrophysical origin reported by IceCube which are visible to ZTF and can be observed promptly. Those alerts not observed by ZTF are summarised in Table 12.2. Of those 23 alerts not followed up by ZTF, the primary reasons were proximity to the Sun (8/23), alerts with poor localisation and low astrophysical probability (6/23) and alert retraction (4/23). For events which were reported with estimates of astrophysical probability*, we chose not to follow up those that had both low astrophysical probability (< 50%) and large localisation regions (> 10 sq. deg.).

[2019ICRC...36.1021B]:
2019ICRC...36.1021B
(2019ICRC...36.1021B),
2019ICRC...36.1021B

Each neutrino localisation region can typically be covered by one or two ZTF observation fields. Multiple observations are scheduled for each field, with both *g* and *r* filters, and a separation of at least 15 minutes between images. These observations typically last for 300 s,

* This value was not reported for high-energy starting events (HESE) under the old IceCube alert selection, nor for one recent alert, IC200107A, that was identified outside of the standard alert criteria [stein:gcn26655].

[stein:gcn26655]: stein:gcn26655
(stein:gcn26655), stein:gcn26655

Table 12.2: Summary of the 23 neutrino alerts that were not followed up by ZTF since survey start on 2018 March 20. Of these, 4/23 were retracted, 11/23 were inaccessible to ZTF for various reasons, 6/23 were deemed alerts of poor quality, while just 2/23 were alerts that were missed although they passed our criteria.

Cause	Events
Alert Retraction	IC180423A[IC180423A], IC181031A[IC181031A] IC190205A[IC190205A], IC190529A[IC190529A]
Proximity to Sun	IC180908A[IC180908A], IC181014A[IC181014A] IC190124A[IC190124A], IC190704A[IC190704A] IC190712A[IC190712A], IC190819A[IC190819A] IC191119A[IC191119A], IC200227A[IC200227A]
Low Altitude	IC191215A[IC191215A]
Southern Sky	IC190331A[IC190331A], IC190504A[IC190504A]
Poor Signalness & Localisation	IC190221A[IC190221A], IC190629A[IC190629A] IC190922A[IC190922A], IC191122A[IC191122A] IC191204A[IC191204A], IC191231A[IC191231A]
Bad Weather	IC200120A[IC200120A , IC200120A_2]
Telescope Maintenance	IC181023A[IC181023A]

with a typical limiting magnitude of 21.0^m . ToO observations are typically conducted on the first two nights following a neutrino alert, before swapping to serendipitous coverage as part of the public survey. We search ZTF data both preceding and following the arrival of the neutrino. Our coincidence criteria are that an object lie within the 90% localisation region reported by Icecube in a GCN circular, and must have been detected at least once following the neutrino arrival time. These cuts typically yield ~ 0.2 candidates per square degree of sky. Promising candidates are prioritised for spectroscopic classification, to confirm or rule out a possible association with a given neutrino.

A selection of highlighted results are given below. A further candidate, AT2019dsg, is described in Chapter 13.

PKS 1502+106

As referenced in 11

SN2019pqh

As introduced in Chapter 11, follow-up of IC190922B by ZTF identified a candidate supernova ZTF19abxtupj/AT2019pjh [[2019ATel13125....1S](#)]. As outlined in chapter 10, neutrino emission has been predicted for core-collapse supernovae from either choked jets or interacting supernovae. SN2019pjh was not consistent with the former scenario, because it was detected prior to the neutrino. However, it was close to peak, as shown in the lightcurve in Figure 12.1. This was the first young supernova found in coincidence with a high-energy neutrino, which is interesting because CSM neutrino emission .

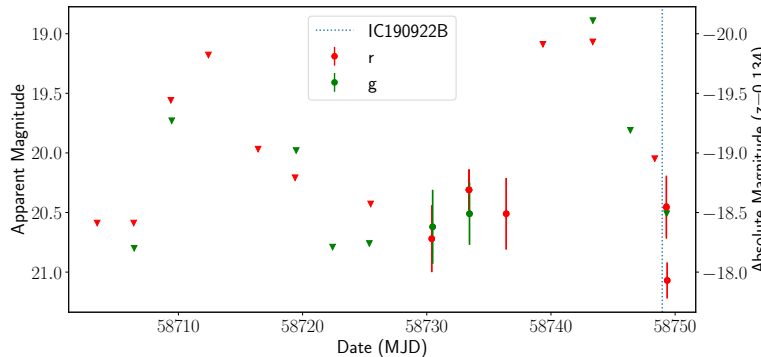


Figure 12.1: ZTF lightcurve of SN2019pqh, with observations in g and r band. The arrival time of the neutrino on 2019 September 22 is marked with a dotted line, and the supernova is detected in the subsequent ToO observations.

This object had first been detected on A subsequent classification of the object as a Type II supernova was reported by ePESSTO (cite).

A high-resolution spectrum of the object was obtained by De Sharma on 2019 September 28, using the (LRIS) spectrograph at the Keck 1 observatory (see Figure 12.2). The host galaxy, clearly visible in Figure N, had a spectroscopic redshift of $z=0.134$ measured by the Sloan (SDSS). Peaks are clearly visible in the spectrum matching hydrogen lines for this redshift, confirming that the transient is indeed coincident with the apparent host galaxy.

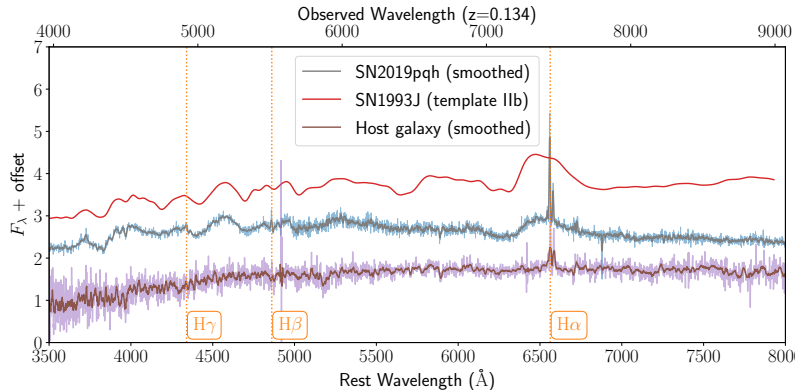


Figure 12.2: Spectrum of SN2019pqh, taken on x. The prominent Balmer lines are highlighted in orange, from which a redshift of 0.134 is derived. A template-matching classification using SNID yields a match to a Type IIb supernova (SN1993J) 2 days before peak cite.

12.3 Gravitational Waves and Gamma-ray Bursts

In contrast to neutrinos, follow-up of GW and GRB triggers is more akin to searching for a needle in a haystack. The localisations tend to be much larger than for neutrinos, but with the well-defined aim of finding kilonovae. In this case, we at least know what our needle looks like. GW170817 provided an observational confirmation of theoretical predictions of kilonovae, namely that they are faint, fast-evolving, red transients which are generated following mergers of neutron stars. Though a trigger event may cover several hundred or thousand square degrees, these constraints enable us to efficiently reject the vast majority of candidates. Additional temporal coincidence is ensured by requiring that candidates are not detected prior to merger/burst, and

spatial coincidence can be ensured using trigger probability skymaps integrated out to predefined confidence intervals (typically 90% or 95%). Unique among triggers, GW events are also typically reported with estimated distance ranges derived from template-matching. For candidates which have a resolved host galaxy, we can determine their distance using spectroscopic surveys such as SDSS, as well as photometric redshift estimates, and veto those candidates lying outside the desired distance range.

The third observing run of the LIGO/VIRGO (O3) extended from X to y, and for this period ZTF has followed-up LVC GW triggers. In this period, there were BNs candidates and Y BBH candidates.

There have been some predictions of EM signatures for BBH events...

13 AT2019dsg and IC191001A

On 2019 October 1, the IceCube Neutrino Observatory reported the detection of a ~0.2 PeV neutrino, IC191001A, with a 59% probability of being of astrophysical origin [stein:gcn25913] (see Chapter 11). Seven hours later, the direction of the incoming neutrino was observed by ZTF as part of our neutrino follow-up program. The data was processed by our multi-messenger pipeline (see Chapter 12) and the radio-emitting tidal disruption event AT2019dsg was identified as a candidate neutrino source [2019ATel13160....1S].

13.1 Discovery of AT2019dsg

AT2019dsg was discovered by ZTF on 2019 April 9 under the name *ZTF19aapreis*, and reported on 2019 April 22 as a likely extragalactic transient by AMPEL [2019TNSTR.615....1N]. AT2019dsg was publicly classified as a TDE on 2019 May 13 by ePESSTO+ on the basis of its optical spectrum [2019ATel12752....1N]. All candidate TDEs identified by ZTF are named after characters from HBO series *Game of Thrones*. As the nth candidate TDE, AT2019dsg was given the official nickname of *ZTF-BranStark* [2020arXiv200101409V].

Radio emission was tentatively reported on 2019 May 23 by [\[2019ATel12798....1S\]](#), and confirmed on 2019 July 26 by e-MERLIN [2019ATel12960....1P]. The potential neutrino association was reported on 2019 October 2 [2019ATel13160....1S]. In addition to object [2019ATel13160....1S], as part of a systematic ZTF search for TDEs [2020arXiv200101409V/2019ATel13160....1S], the association with IC191001A prompted additional follow-up [2019ATel13160....1S]

13.1 Discovery of AT2019dsg	63
13.2 Observation of AT2019dsg	64
Optical/UV	64
X-ray	65
Radio	66
Gamma-ray	69
Spectroscopy	70
13.3 Neutrino emission from AT2019dsg	72
13.4 Probability of Chance Coincidence	74
13.5 Implications of AT2019dsg	75

[2019TNSTR.615....1N]:
2019TNSTR.615....1N
(2019TNSTR.615....1N)
[2019ATel12752....1N]
2019TNSTR.615....1N
2019ATel12752....1N
(2019ATel12752....1N)
2019ATel12752....1N

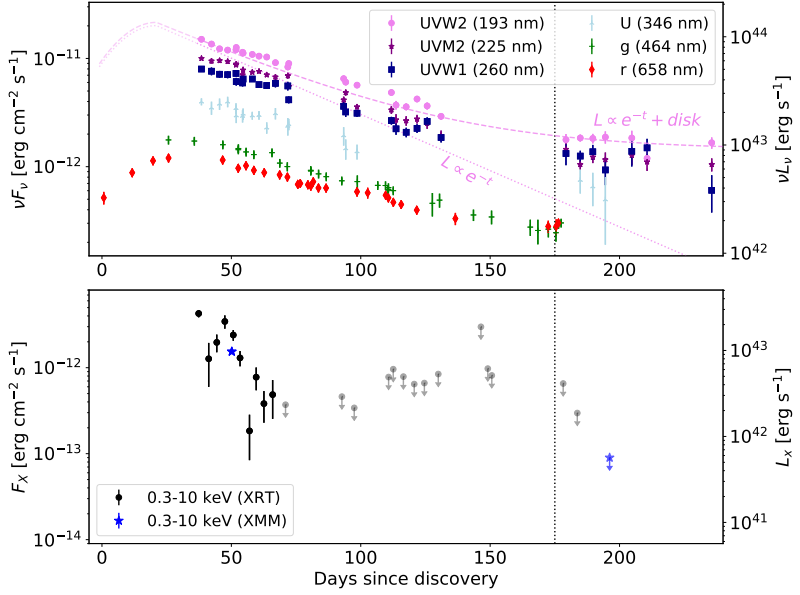


Figure 13.1: Multi-wavelength lightcurve of AT2019dsg. Error bars represent 1σ intervals. The upper panel shows the optical photometry from ZTF, alongside UV observations from *Swift*-UVOT. The plateau luminosity is a factor of 10 brighter in UVW2 than the pre-disruption baseline of the host galaxy. The lower panel shows the integrated X-ray energy flux, from observations with *Swift*-XRT and *XMM-Newton*, in the energy range 0.3–10 keV. Arrows indicated 3σ upper limits. The vertical dotted line illustrates the arrival of IC191001A.

13.2 Observation of AT2019dsg

Optical/UV

The optical/UV continuum of AT2019dsg is well described by a single blackbody photosphere with a near-constant temperature [2020arXiv200101409V] of $10^{4.59 \pm 0.02}$ K and radius of $10^{14.59 \pm 0.03}$ cm. The peak luminosity of $10^{44.54 \pm 0.08}$ erg s $^{-1}$ is in the top 10% of the 40 known optical TDEs to date [2020arXiv200101409V], and the temperature is in the top 5%. By the time of the neutrino detection, the optical/UV luminosity appeared to have reached a plateau (see Figure 13.1). Such plateaus are common in TDEs and interpreted as emission from the outer part of an accretion disk [2019ApJ...878...82V, 2020MNRAS.492.5655M], but typically occur a few years after peak. The rapid appearance of an accretion-disk plateau would be expected for disruptions around higher-mass SMBHs. Indeed the total mass of the host galaxy of AT2019dsg is in the top 10% of all optical TDE hosts. Assuming 50% of the host mass is in the bulge, we estimate [2013ApJ...764..184M] a black hole mass of $\sim 3 \times 10^7 M_\odot$.

Prior to the detection of IC191001A, AT2019dsg had already been repeatedly detected by ZTF P48 telescope as part of the public MSIP survey, most recently on 2019 September 28. These data were supplemented by photometric observations from the 2m Liverpool Telescope [2004SPIE.5489..6] and SEDM [Blagorodnova18, Rigault19] photometry [fst+2016] obtained using the P60 telescope on Mt Palomar. ToO observations of the neutrino localisation field began on 2019 October 1, 7.4 hours after the neutrino detection. A second set of observations were performed the following night. In all of these images AT2019dsg was clearly visible.

UV observations of AT2019dsg were conducted as part of a systematic survey of UV properties of all ZTF-identified TDEs [2018ApJ...852...72V], using the UltraViolet/Optical Telescope [2005SSRv..120...95R] (UVOT) on board the *Neil Gehrels Swift Observatory* (*Swift*) [2004ApJ...611.1005G].

Data were reduced with `uvotsource` using an aperture of 7" to capture the entire galaxy (the host flux density was subtracted based on the best-fit galaxy model[[2018ApJ...852...72V](#)] and uncertainties on this baseline are propagated into the reported UVOT difference photometry). The first UV observation was performed 15 days after the optical peak on 2019 May 17, and a bright source spatially coincident with the TDE was detected. Subsequent observations continued at a cadence of 2–3 days, up to 2019 September 7. In this period, AT2019dsg continued to steadily dim. An additional observation occurred shortly before the neutrino detection on 2019 September 27. Follow-up observations were then triggered by the identification of a possible association with IC191001A[[2019ATel13160...1S](#)], beginning on 2019 October 5.

The optical/UV data are summarised in Table ???. We note that in the final ZTF observations, the source appears to redden in the optical bands. This could be a signature of reverberation due emission from dust heated by the TDE[[2016ApJ...829...19V](#), [2016MNRAS.458..575L](#)]; this dust can reach a temperature of ~ 2000 K. An important caveat is that the contrast between the transient emission and the host is very small for these late-time optical detections, so the residuals in the difference image may need to be corrected to account for small systematic offsets. That can only be investigated when the images for this portion of the public survey are published as part of the next ZTF data release. We note that the UV observations are not subject to the same uncertainty because even at late times the transient UV flux is about an order of magnitude brighter than the host baseline.

X-ray

AT2019dsg was also detected in X-rays, beginning 37 days after discovery. Though the first X-ray observation indicated a bright source, with a high X-ray to optical ratio of $L_X/L_{\text{opt}} \sim 0.1$, this X-ray flux faded extremely rapidly, as shown in Figure 13.1. This rate of decline is unprecedented, with at least a factor of 50 decrease in X-ray flux over a period of 159 days. Similar to the optical/UV emission, the observed X-ray spectrum is consistent with thermal emission, but from a blackbody of temperature $10^{5.9}$ K (0.072 ± 0.005 keV) and, assuming emission from a circular disk, a radius $\sim 2 \times 10^{11}$ cm. As for most X-ray-detected TDEs[[2017ApJ...838..149A](#), [2019MNRAS.487.4136W](#), [2019ApJ...872..198V](#)], the blackbody radius appears much smaller than the Schwarzschild radius ($R_S \sim 10^{13}$ cm) inferred from the galaxy scaling relation[[2013ApJ...764..184M](#)]. Small emitting areas can arise from an edge-on orientation, because the relativistic velocities at the inner disk can Doppler boost a large area of the disk out of the X-ray band. Since our observations probe close to the Wien tail of the spectrum, a small temperature decrease due to absorption would also yield a significantly underestimated blackbody radius and luminosity[[2019ApJ...872..198V](#)]. The exponential decrease of the flux could be caused by cooling of the newly-formed TDE accretion disk[[2020MNRAS.492.5655M](#)] or increasing X-ray obscuration.

AT2019dsg was first observed in X-rays on 2019 May 17 by the X-Ray Telescope (XRT)[[2005SSRv..120..165B](#)], also on board *Swift*[[2004ApJ...611.1005G](#)], as part of a program to categorise the X-ray properties of TDEs. AT2019dsg was detected at high significance at this epoch, with a measured energy flux of $F_X \sim 4 \times 10^{-12}$ erg cm $^{-2}$ (0.3–10 keV). Observations continued with a cadence of 2–3 days, and indicated a sharply-declining X-ray flux. The source was last detected on 2019 June 14, and not detected again in any of the following observations continuing until 2019 September 7. An additional observation was performed with the *X-ray Multi-Mirror Mission* (*XMM-Newton*) telescope on 2019 May 30, in the range 0.3–10 keV. The *XMM-Newton* EPIC-pn observations (programs 082204 and 08425; P.I. Gezari) were taken in Wide window Thin1 filter mode and reduced using standard techniques with the *XMM-Newton*[[2001A&A...365L...1J](#)] Science Analysis System (SAS). The source extraction region was a circle of radius 35 arcsec at the location of the optical transient in the X-ray image, and the background was measured using a 108-arcsec circular region (shown in Figure 13.2). The XMM spectrum was binned using the GRPPHA command, such that there were at least 20 counts contained in each bin. It was then fit ($\chi^2/\text{dof} = 59.26/65$) with the disk blackbody (diskbb) model with Galactic[[HI4PI2016](#)] and intrinsic ($N_{\text{H}} \sim 4 \times 10^{20}$ cm $^{-2}$) absorption described using the phabs model in XSPEC v12.9.1[[1996ASPC..101...17A](#)]. The flux was consistent with those of *Swift*-XRT, and provided a high signal-to-noise X-ray spectrum well-fitted with a single disk temperature of $T_{\text{disk}} = 10^{5.9}$ K (0.072 ± 0.005 keV), shown in Figure 13.3. Following the identification of AT2019dsg as a candidate counterpart to IC191001A[[2019ATel13160....1S](#)], additional X-ray observations were triggered. AT2019dsg was again not detected, with the first *Swift*-XRT observation occurring on 2019 October 5. An additional XMM observation on 2019 October 23 yielded a deep upper limit of 9×10^{-14} erg cm $^{-2}$ s $^{-1}$ (0.3–10 keV) using the same thermal model, computed at the 3σ confidence level using the XMM SAS/HEASARC command eregionanalyse.

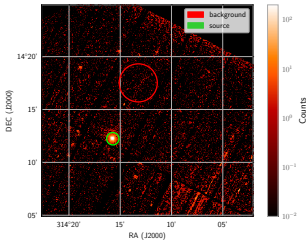


Figure 13.2: X-ray count map from *XMM-Newton* (50 days after discovery). The green circle indicates the source region, while the red circular region was used to measure the background. The best-fit position derived from optical observations is spatially-coincident with the center of the X-ray source region.

Radio

Radio observations shown in Figure ?? reveal a third distinct spectral component, namely synchrotron emission from non-thermal electrons. We model this emission with a conical geometry as expected for outflows (e.g., jets or winds) that are launched from—and collimated by—the inner parts of flared accretion disks that emit close to the Eddington limit. Given that electrons are typically accelerated with much lower efficiency than protons in astrophysical accelerators[[2012A&A...538A..81M](#)], we assume that they carry 10% of the energy carried by relativistic protons ($\epsilon_e = 0.1$). We further assume that the magnetic fields carry 0.1% of the total energy ($\epsilon_B = 10^{-3}$), as indicated by radio observations of other TDEs[[2018ApJ...854...86E](#)] and supernovae[[2013MNRAS.436.1258H](#)]. For a half-opening angle, ϕ , of 30° we find $R = 1.5 \times 10^{16}$ cm in our first epoch (41 days after discovery), increasing to $R = 7 \times 10^{16}$ cm shortly after the neutrino detection (177 days after discovery). These radii scale[[2013ApJ...772...78B](#)] as $R \propto [1 - \cos(\phi)]^{-8/19}$. The implied

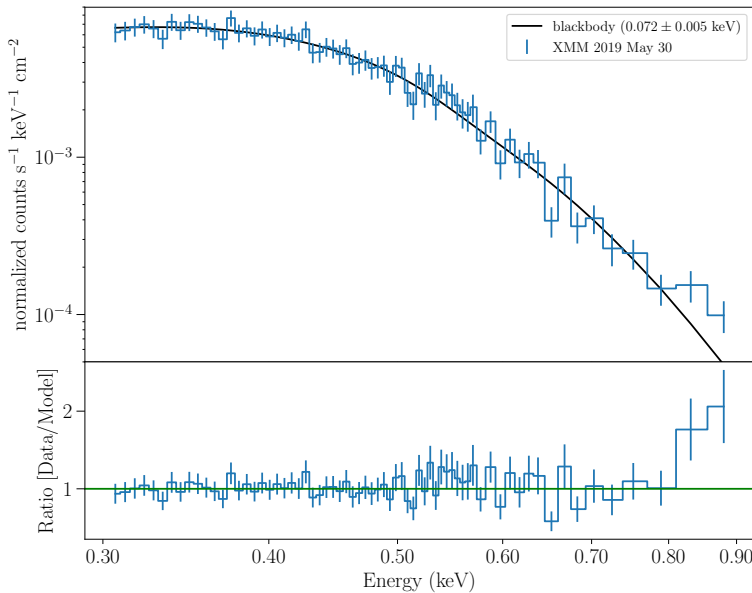


Figure 13.3: Soft X-ray spectrum of AT2019dsg measured by *XMM-Newton*, fitted with an absorbed disk blackbody model. Error bars represent 1σ intervals.

expansion velocity is roughly constant at $v/c = \dot{R}/c = 0.12 \pm 0.01$ during the first three epochs, with an acceleration to $v/c = 0.21 \pm 0.02$ for the last epoch. These are the velocities of the synchrotron-emitting region, and thus provide a lower limit to the velocity at the base of the outflow. Indeed even the hotspots of relativistic jets from active galaxies that are frustrated by gas in their host galaxy are typical observed[2003PASA...20...69P] to have subrelativistic expansion velocities of $\sim 0.1c$.

The inferred outflow energy, E , shows a linear increase from $2.5 \times 10^{49} \text{ erg}$ to $2 \times 10^{50} \text{ erg}$ (Figure ??), which is not expected in models[2016ApJ...819L..25A, 2016ApJ...827..127K] of TDE radio emission that involve a single injection of energy. While some scenarios can yield an increase in inferred energy from a single energy injection, none of these are consistent with the full set of observed properties. First, a single ejection with a range of velocities could explain the observed linear increase of energy with time (the slower ejecta arrive later), but is incompatible with the increasing velocity. Second, an increase of the efficiency for conversion of Poynting luminosity to relativistic particles is unlikely because the target density that is available to establish this conversion is decreasing. And finally, an increase of solid angle that emits to our line of sight is only expected for relativistic outflows that decelerate. Instead, for AT2019dsg, the observations suggest the presence of a central engine that yields continuous energy injection through a coupling of accretion power to the radio emission[2018ApJ...856....1P], with acceleration in the final radio epoch due to a decrease in the slope of the ambient matter density profile.

Four observations of AT2019dsg were performed with the Karl G. Jan- sky Very Large Array (VLA) under project code 19A-395 (PI: van Velzen), on 2019 May 22, June 19, August 8 and October 5. The array was in its moderately-extended B configuration (maximum baseline 11 km) for

the first two epochs, and in its most extended A-configuration (maximum baseline 36 km) for the final two epochs. Our first epoch, on May 22, was a detection experiment, and we observed only in the 8–12 GHz band. Having established the presence of radio emission, we observed over a broader range of frequencies in the subsequent three epochs, using the 2–4 GHz, 4–8 GHz, and 8–12 GHz bands. We used 3C 48 as a bandpass and flux density calibrator on May 22, and 3C 286 for the other three epochs. We used the nearby extragalactic sources ICRF J204945.8+100314 (at 4–8 and 8–12 GHz) and ICRF J203533.9+185705 (at 2–4 GHz) to determine the complex gain solutions, which were interpolated to AT2019dsg. We used the Common Astronomy Software Application (CASA)[McMullin2007] Calibration pipeline (v5.4.1) to perform external gain calibration, and after removing residual radio frequency interference, we imaged the data within CASA, using Briggs weighting with a robust parameter of 1. We split each baseband into multiple frequency bins for imaging (1 GHz bins above 4 GHz, and 0.5 GHz bins below that) to provide better sampling of the broadband spectrum, allowing more precise constraints on the turnover frequency, and better spectral modelling.

Radio observations of the field of AT2019dsg were also conducted using the AMI Large Array (AMI-LA)[2008MNRAS.391.1545Z, 2018MNRAS.475.5677H]. AMI-LA is a radio interferometer comprised of eight 12.8m-diameter antennas producing 28 baselines that range from 18m up to 110m, which operates with a 5 GHz bandwidth around a central frequency of 15.5 GHz. We observed AT2019dsg on several epochs (see Table ??) for four hours each. Initial data reduction, editing, and calibration of the phase, and flux density, was carried out using `reduce_dc`, a customized AMI data reduction software package[2015MNRAS.453.1396P]. Phase calibration was conducted using short interleaved observations of ICRF J205135.5+174336, while for absolute flux density calibration we used 3C 286. Additional flagging and imaging were performed using CASA. All of our observations showed a source consistent with the location of AT2019dsg. We used the CASA task IMFIT to find the source flux and position.

Further observations of AT2019dsg were conducted with the South African MeerKAT telescope, on 2019 June 19, July 29, October 5, and November 30, with each session being ~ 2 h long. We used ICRF J193925.0-634245 as a flux-density calibrator, and ICRF J213032.8+050217 as a phase and amplitude calibrator. The initial calibration was done using the IDIA MeerKAT pipeline*, which is implemented in CASA. The observed band was 860 MHz wide and centred on 1280 MHz. We imaged the whole primary beam ($\sim 1^\circ$) using the CLEAN algorithm (CASA: `tclean`) in order to remove sidelobes from the many (unrelated) sources within the primary beam. The total CLEAN flux density in the field was ~ 1 Jy, and the peak brightness in the images was about 48 mJy beam $^{-1}$ (not related to AT2019dsg). Since residual small calibration errors dominated the image rms background in the initial images, we self-calibrated the data in both phase and amplitude, with the mean amplitude gain being fixed at unity to minimise any drifting of the flux-density scale. The resolution is slightly different in each epoch,

* <https://idia-pipelines.github.io/docs/processMeerKAT>

but was $\sim 11''$ north-south, and $\sim 6''$ east-west. Image rms background levels also varied, ranging between 25 and $32 \mu\text{Jy beam}^{-1}$. There was no sign of extended emission or confusing sources near AT2019dsg. The flux density was determined by fitting an elliptical Gaussian with the same geometry as the restoring beam to the images.

The measured flux densities from our radio observations are reported in Table ???. For all radio observations, the reported uncertainties include both the image background rms and a 5% fractional calibration uncertainty, added in quadrature.

Gamma-ray

We analysed data from the *Fermi* Large Area Telescope (*Fermi*-LAT)[2009ApJ...697.1071A], sensitive to gamma rays with energies from 20 MeV to greater than 300 GeV. During its sky-survey operations, the pair-conversion telescope *Fermi*-LAT scans the entire sky about every three hours, and can monitor the variable gamma-ray sky over short and long timescales. We studied the region of AT2019dsg in three different time intervals, motivated by the multi-wavelength behavior of the source. The first interval (G1) includes 130 days of observations that include the peak of the optical emission from 2019 April 4 to 2019 August 12. The second one (G2) spans 2019 August 12 to 2019 November 20 and covers the UV plateau and the peak of the radio emission. The third period (G3) integrates the whole period between the start of G1 up to 2020 January 31. We use the photon event class from Pass 8 *Fermi*-LAT data (P8R3_SOURCE), and select a $15^\circ \times 15^\circ$ Region of Interest (RoI) centered on the AT2019dsg position derived from optical observations, with photon energies from 100 MeV to 800 GeV. We use the corresponding LAT instrument response functions P8R3_SOURCE_V2 with the recommended spectral models *gll_iem_v07.fits* and *iso_P8R3_SOURCE_V2_v1.txt* for the Galactic diffuse and isotropic component respectively. To minimise contamination from gamma rays produced in the Earth's upper atmosphere, we require an instrumental zenith angle $\theta < 90^\circ$ for all events, in addition to the standard data quality cuts suggested by the *Fermi* Science Support Center*. We perform a likelihood analysis, binned spatially with 0.1° resolution and 10 logarithmically-spaced bins per energy decade, using the *Fermi*-LAT ScienceTools package (fermitools v1.0.1) along with the *fermipy* package v0.17.4[2017ICRC...35..824W].

A search was already performed within the 90% error region during both the 1-day and 1-month period prior to the arrival of the high-energy neutrino[garrappa_buson:gcn25932]. No new gamma-ray source was identified, and there was no significant ($\geq 5\sigma$) detection for any source from the fourth *Fermi*-LAT point source catalog (4FGL[2019arXiv190210045T]). Here, we specifically test a point-source hypothesis at the position of AT2019dsg under the assumption of a power-law spectrum. We find $\text{TS}^\dagger = 0$ for all intervals. Upper

* https://fermi.gsfc.nasa.gov/ssc/data/analysis/scitools/data_preparation.html

† TS is twice the difference in the maximum $\log \mathcal{L}$ of an ROI model with and without the source, where \mathcal{L} is the likelihood of the data given the model.

Table 13.1: Gamma-ray energy flux upper-limits for a point-source with power-law index $\Gamma=2.0$ at the position of AT2019dsg integrated over the analysis energy range 0.1-800 GeV.

Interval	MJD Start	MJD Stop	UL (erg cm $^{-2}$ s $^{-1}$)
G1	58577	58707	2.6×10^{-12}
G2	58707	58807	1.2×10^{-11}
G3	58577	58879	2.0×10^{-12}

limits for the energy flux (integrated over the whole analysis energy range) have been derived for a power-law spectrum ($dN/dE \propto E^{-\Gamma}$) with photon power-law index $\Gamma = 2$ and are listed in Table 13.1 along with the respective time intervals.

In all three time intervals, we detect a new, non-catalogued gamma-ray emitter in the RoI at a significance $\geq 5\sigma$. This source lies just outside the IC191001A 90% error region, as indicated in Figure 13.4. The source, which we label *Fermi*-J2113.8+1120, is likely the gamma-ray counterpart of the radio-loud object GB6 J2113+1121, classified as a flat-spectrum radio quasar with redshift $z = 1.63$ [2013ApJ...767...14P]. The detection of an unrelated gamma-ray blazar within the neutrino uncertainty area is consistent with the background estimation. On average 1.5 4FGL gamma-ray blazars are expected in 20 sq. deg. In addition, a lightcurve analysis (Figure 13.5) reveals that the source is not significantly detected in gamma rays when IC191001A was detected. The lag between the closest significant detection of the source and the neutrino arrival was approximately ~ 1 month. Such a lag is disfavored by recent studies on the temporal behavior of hadronic processes in blazars[2015ApJ...802..133D, 2019NatAs...3...88G], suggesting that the blazar is unlikely producing the neutrino. Hence, given the lack of any obvious connection between the gamma-ray observations of *Fermi*-J2113.8+1120 and IC191001A, we do not discuss this source any further.

The HAWC observatory also reported a search for transient gamma-ray emission on short timescales in the localisation of IC191001A[ayala:gcn25936], and set a limit for their most significant position at 95% confidence of $E^2 dN/dE = 3.51 \times 10^{-13} (E/\text{TeV})^{-0.3} \text{ TeV cm}^{-2} \text{ s}^{-1}$, in the energy range 300 GeV to 100 TeV, for the period from 2019 September 30 05:46:52 UTC to 2019 October 02 06:03:29 UTC. We note that this search covered a relatively large region of the sky, and thus had a large associated trial factor. A dedicated search at the position of AT2019dsg would be more sensitive, especially one that additionally targeted the longer period over which the central engine is active.

Spectroscopy

AT2019dsg was discovered by ZTF on 2019 April 9 under the name [2019TNSTR.615....1N]F19aapreis, and publically reported as a [2019TNSTR.615....1N], 2019TNSTR.615....1N and was classified as a TDE on the basis of its optical spectrum[2019ATel12752....1N] (2019TNSTR.615....1N), 2019TNSTR.615....1N With a measured redshift of $z = 0.051$, implying a luminosity distance $D_L \approx 230$ Mpc assuming a flat cosmology with $\Omega_\Lambda = 0.7$ and $H_0 = 70$ km s $^{-1}$ Mpc $^{-1}$.

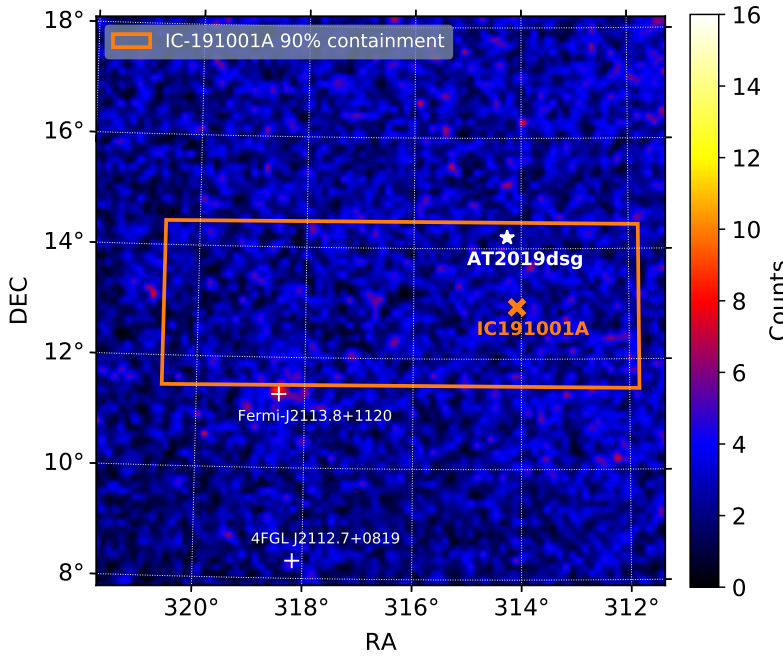


Figure 13.4: LAT counts map of the Region Of Interest (ROI) in the integrated search period G3, showing the IC191001A 90% localisation region in green. The neutrino best-fit position is marked with a green ‘x’. Two gamma-ray sources are significantly detected ($\geq 5 \sigma$) in the ROI but outside the neutrino uncertainty region as marked with white crosses. There is no excess consistent with the position of AT2019dsg.

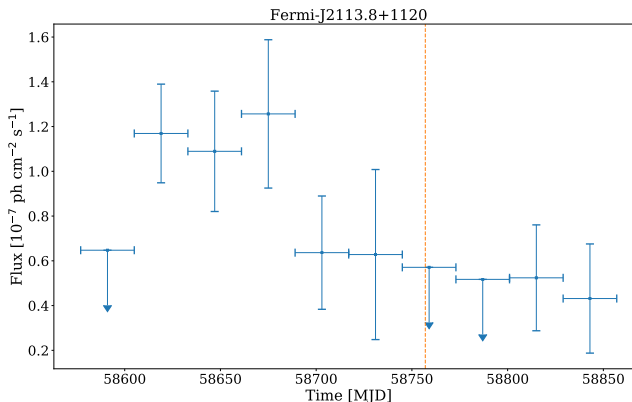


Figure 13.5: LAT lightcurve in the 0.1-800 GeV energy range for the source Fermi-J2113.8+1120 in the time interval G3, with evenly spaced binning of 28 days. Vertical error bars represent 1σ intervals, horizontal bars denote bin width. 2σ upper limits are shown for bins with $TS \leq 9$. The orange dashed vertical line marks the arrival time of IC-191001A. Since this source lies outside the reported 90% error region (see Figure 13.4), and given that the LAT lightcurve shows no obvious correlation with the neutrino arrival time, we conclude that it is unlikely to be associated with the neutrino.

AT2019dsg was first classified as a TDE by ePESSTO+ on 2019 May 13 [2019ATel12752....1N], and the redshift of AT2019dsg was measured to be $z = 0.051$. Further high-resolution spectroscopic observations were conducted using the De Veny Spectrograph on the 4.3m Lowell Discovery Telescope (LDT, PI: Gezari), the Kast Double Spectrograph on the 3m Lick Observatory Shane Telescope (Lick, PI: Foley) [Miller93], and the Low Resolution Imaging Spectrograph on the 10m Keck Telescope (Keck, PI: Graham) [Oke95], with the most recent spectrum on 2019 September 25. These spectra confirm that AT2019dsg belongs to the common spectroscopic class of TDEs with Bowen fluorescence emission lines and broad H α emission lines [2020arXiv200101409V]. We note that the Ca triplet is also clearly visible in our late-time spectra (rest-frame 8498 Å, 8542 Å and 8662 Å), so the SMBH mass could in principle be inferred more precisely using higher-resolution spectroscopy of this feature [2005MNRAS.359..765G]. Following the identification of AT2019dsg as a candidate neutrino source, additional high-resolution spectra of the source were taken with the 200in Hale Telescope Double Spectrograph at Palomar Observatory (P200, PI: Kasliwal & Kulkarni) on 2019 October 3 and again with Lick on 2019

October 5 and 2019 October 29 (shown in Figure 13.6). There is no evidence of any significant spectral evolution between these spectra and the most recent pre-neutrino spectrum from 2019 September 25, and the spectral evolution of AT2019dsg is consistent with that of other TDEs[2020arXiv200101409V].

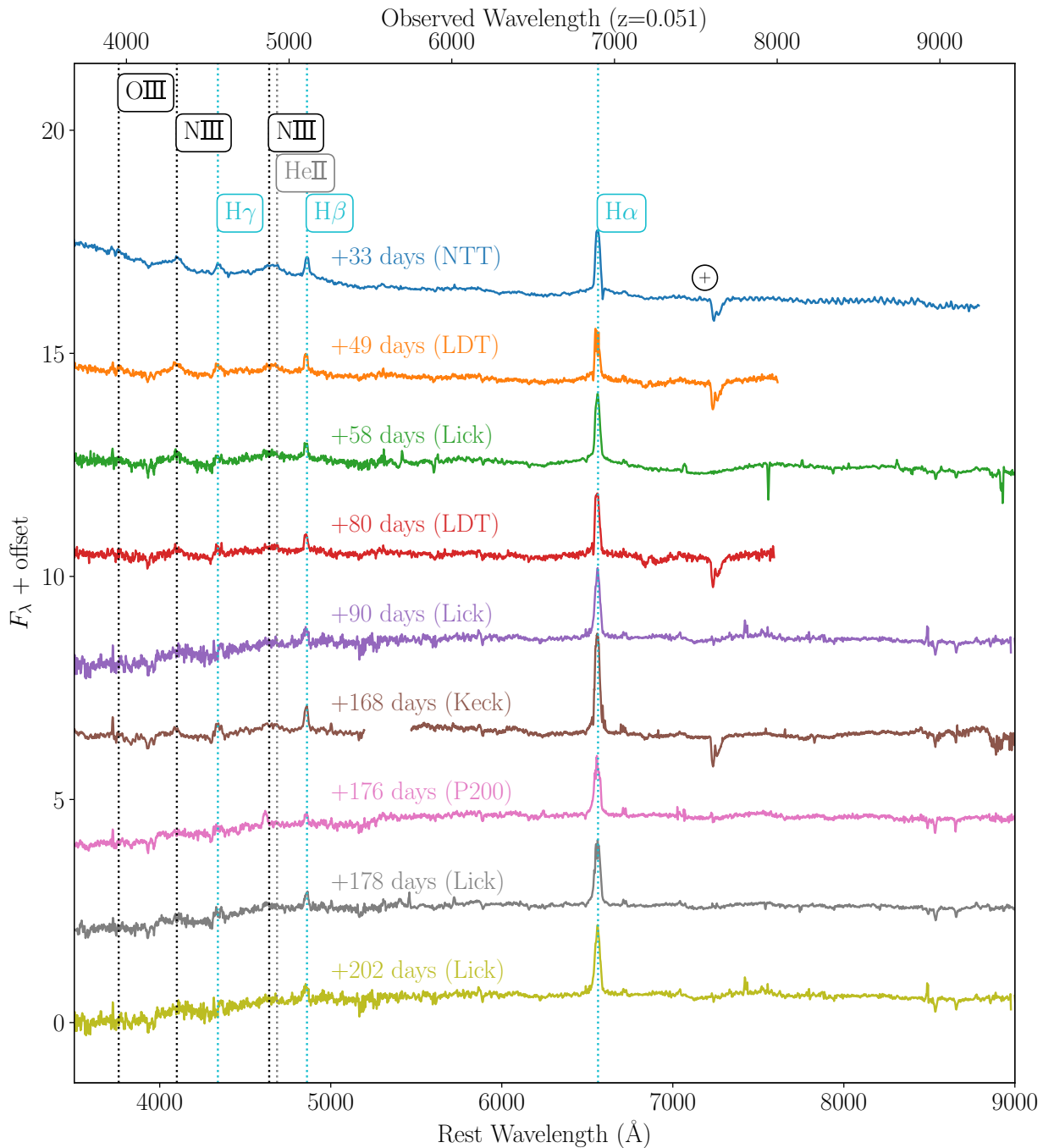


Figure 13.6: The spectroscopic evolution of AT2019dsg, beginning with the publicly available classification spectrum taken with the NTT[2019ATel12752....1N], and further spectra from LDT, Lick, Keck and P200. The Balmer lines are highlighted in cyan, the HeII lines in gray, and the Bowen fluorescence lines (OIII at 3760 \AA , NIII at 4100 \AA and 4640 \AA) in black. Telluric lines are marked with +.

13.3 Neutrino emission from AT2019dsg

With this strong evidence for three distinct emission zones derived purely from multi-wavelength observations, we consider whether this picture is consistent with AT2019dsg being the source of the neutrino IC191001A. In particular, neutrino production requires protons to be accelerated to sufficiently high energies, and to collide with a suitably abundant target. The detection of a single high-energy neutrino implies a mean expectation in the range $0.05 < N_{\nu,\text{tot}} < 4.74$ at 90% confidence, where $N_{\nu,\text{tot}}$ is the cumulative neutrino expectation for all TDEs that ZTF has observed. AT2019dsg emits $f_{\text{bol}} \sim 0.16$ of the population bolometric energy flux, and if we take this as a proxy for neutrino emission, we would expect $0.008 \lesssim N_{\nu} \lesssim 0.76$ for this source.

Radio observations confirm that particle acceleration is indeed occurring, and that this continues without decline through to the detection of the neutrino at ~ 180 days post-discovery. Given that neutrinos typically take a fraction $\eta_{p\nu} \sim 0.05$ of the parent proton energy, our accelerator must be capable of accelerating protons to at least 4 PeV. We evaluate the Hillas criterion[1984ARA&A..22..425H] that the proton Larmor radius be less than the system size, to determine whether this is possible. We use our estimates for conditions in the synchrotron zone at the time of neutrino detection, with $B \sim 0.07$ G and $R \sim 7 \times 10^{16}$ cm for the near-contemporaneous radio epoch. Taking this as a baseline, we find a maximum proton energy of ~ 160 PeV, far in excess of our requirements. The Hillas criterion can also be satisfied within the engine that powers the radio-emitting outflow because the product BR is not expected to decrease at smaller radii (e.g. $B \propto R^{-1}$ for a toroidal configuration).

The target for neutrino production can be either photons ($\gamma\gamma$ interactions) or protons ($p\gamma$ interactions). For a photon target, neutrino production occurs above an energy determined by the mass of the Δ resonance, m_{Δ} . For a thermal spectrum, of temperature T , we then find $\epsilon_{\nu} \sim \eta_{p\nu}[(m_{\Delta}^2 - m_p^2)/4\epsilon_{\gamma}] \approx 0.3 \times (T/10^5 \text{ K})^{-1}$ PeV. For the UV photosphere of the TDE, we find $\epsilon_{\nu} \sim 0.8$ PeV, while for the compact X-ray source, we find $\epsilon_{\nu} \sim 0.05$ PeV. Both of these values are compatible with the observed neutrino, for which there is a typical uncertainty of one energy decade[2018Sci...361.1378I], so either photon field could serve as a target. For the UV photosphere, we find that the mean free path for the parent proton of a PeV neutrino ($\sim 2 \times 10^{13}$ cm, see SI) is much smaller than the photosphere radius, so the UV photosphere is indeed optically thick. At smaller radii, the X-rays would overtake the UV photons as dominant scattering targets.

In the multi-zone model shown in Figure ??, the thermal photons provide a guaranteed target for pion production. However hadrons could in principle also serve as a target, leading us to consider a single-zone scenario in which the protons are accelerated at the same location as the synchrotron-emitting electrons, with the neutrino spectrum following the same intrinsic energy power law as the protons and electrons. For $p\gamma$ neutrino production, high target densities of

$n_p \sim 1/(\sigma_{pp}R) \sim 10^8 \text{ cm}^{-3}$ would be required for efficient production of neutrinos, where σ_{pp} is the proton-proton cross section and $R \sim 10^{17} \text{ cm}$ is the characteristic size of the radio region at the time of neutrino production. This high density could be provided by the unbound stellar debris, although this component moves with a typical maximum velocity[2016ApJ...827..127K] of $0.05 c$, and therefore the majority of this debris would have to be swept up with the outflow. Alternatively, the density could be provided by pre-existing gas, although since this gas orbits in the sphere of influence of the black hole, it would be challenging to satisfy the upper limits on pre-disruption accretion.

To obtain the expected neutrino flux from this source we have to estimate the energy carried by protons (E_p) that are accelerated above the energy threshold needed to produce high-energy neutrinos. The outflow energy of $2 \times 10^{50} \text{ erg}$ that we derived from the radio observations (Figure ??) represent a lower bound to the energy that is available for particle acceleration in a central engine. Indeed, the total energy budget for a TDE is set by the mass of the disrupted star, with $E_{\text{TDE}} \sim (1/2) 0.1 M_\odot c^2 \sim 10^{53} \text{ erg}$ for a solar-mass star. We will assume 1% of this total energy budget is carried by relativistic protons, $E_p \sim 10^{51} \text{ erg}$. The total energy in muon neutrinos would then be $E_{\nu, \text{tot}} = (1/8)E_p \sim 10^{50} \text{ erg}$ for efficient optically-thick pion production, after accounting for the pion decay yield and subsequent neutrino flavour oscillations. Convoving this implied energy $E_{\nu, \text{tot}}$ with the effective area, A_{eff} , of IceCube's high-energy neutrino alert selection[2019ICRC...36.1021B], we estimate the expected number of neutrino alerts. Approximating the sharply-peaked $p\gamma$ neutrino spectrum as a monoenergetic flux anywhere between $0.2 \text{ PeV} \lesssim \epsilon_\nu \lesssim 1 \text{ PeV}$, we find $N_\nu = (E_{\nu, \text{tot}} / \epsilon_\nu)(A_{\text{eff}} / 4\pi D_L^2) \sim 0.03$. Thus any optically-thick $p\gamma$ scenario would be sufficient to produce the neutrino under these assumptions.

In contrast to a peaked $p\gamma$ neutrino spectrum, for pp production the neutrinos would instead follow a power law. Many of these neutrinos would then fall below the threshold of IceCube's alert selection. The associated gamma rays would however fall within the sensitive range of gamma-ray telescopes, so this scenario could be securely identified through a joint neutrino-gamma ray signal. While no gamma-ray emission was measured using the *Fermi*-LAT telescope for AT2019dsg (see SI), gamma-ray Cherenkov telescopes may be sensitive to the expected gamma-ray signal, and the corresponding low-energy (TeV) neutrino emission could confirm a hadronic origin. Conversely, the high optical depth of the UV photosphere would absorb any gamma rays accompanying $p\gamma$ neutrino emission[2016PhRvD..93h3005W]. Some contribution from gamma-dark sources is required to explain the large astrophysical neutrino flux[2016PhRvL.116g1101M].

13.4 Probability of Chance Coincidence

AT2019dsg was thus quickly identified as a promising candidate neutrino source [2019ATel13160....1S]. Given that there are typically $\lesssim 2$ radio-emitting TDEs in the entire northern sky at any one time, we find that in the 80 sq. deg. of sky observed during the eight neutrino follow-up campaigns by ZTF up to March 2020, the probability of finding a radio-detected TDE by chance is 0.5%. With the second highest bolometric energy flux of all seventeen TDEs detected by ZTF, the probability of finding a TDE at least as bright as AT2019dsg by chance is just 0.2% (see SI).

During the first 18 months of survey operations, ZTF identified 17 TDEs [2020arXiv200101409V], distributed over 28000 deg of observed sky (the ZTF survey footprint, after removing sources with a Galactic latitude $|b| < 7$). Of these TDEs, each was typically detected for ~ 6 months [2020arXiv200101409V]. We thus estimate that the density of ZTF-detected TDEs is approximately 2.0×10^{-4} per sq. deg. of sky in the survey footprint at any given time. Our follow-up pipeline requires that any candidate be detected by ZTF in ToO observations following a neutrino, in order to establish temporal coincidence. We assume that our neutrino pipeline does not have a significantly higher selection efficiency than the dedicated ZTF program to identify TDEs [2020arXiv200101409V], and thus that the latter provides a reasonable estimate on the background rate of TDEs passing our pipeline.

Those TDEs with radio detections are considered the most promising candidates for neutrino production, as the radio emission serves as a tracer for the particle acceleration required in neutrino sources. We can consider the fraction of TDEs which would additionally be detected in radio, assuming that all could be observed. Among the ZTF sample of confirmed TDEs, we undertook radio follow-up observations with the VLA for 6, of which 2 were detected. Taking this implied radio-emitting fraction of 33%, we then find a final density of 5.9×10^{-5} radio-emitting TDEs per sq. deg. of surveyed sky.

As shown in Chapter 12 (Table 12.1), ZTF has followed-up eight neutrinos up to January 2020, and has covered a combined localisation region of 81.05 sq. deg. With this sky area, the expected number of coincident radio-detected TDEs across all of our neutrino follow-up campaigns is 4.8×10^{-3} . The Poisson probability of observing at least one chance-coincidence radio-emitting TDE during our entire neutrino follow-up campaign is thus 4.8×10^{-3} .

As radio follow-up observations of ZTF TDEs were biased towards those most likely to be detectable, this estimate is an overly conservative one. Because the bolometric energy flux derived from UV/optical observations (i.e., the blackbody luminosity over the square of the distance) serves as a proxy for the non-thermal emission, TDEs which were bright under this metric were preferentially selected for radio observations. To avoid this selection bias, we can instead directly use this bolometric energy flux as a proxy for neutrino flux to identify the most promising candidates for neutrino detection, namely those TDEs which are both nearby and luminous. Of the 17 TDEs observed by ZTF,

AT2019dsg ranks second in this metric. The probability of finding a TDE in our neutrino follow-up campaign with a bolometric energy flux that is at least as high as AT2019dsg is thus 1.9×10^{-3} .

13.5 Implications of AT2019dsg

Given the different neutrino spectrum expectations, a search for accompanying lower-energy neutrinos could be used to probe the conditions at the site of proton interaction. IceCube has already searched for correlations between a sample of TDEs and a neutrino dataset dominated by lower-energy events[[2019ICRC...36.1016S](#)]. Thermal TDEs account for less than 39% of the diffuse astrophysical flux under the assumption of standard candles following a power-law spectrum. This finding is not in tension with the association we have identified, particularly given the low expected neutrino flux we have derived for AT2019dsg. As TDE discovery rates have increased substantially since the previous IceCube analysis[[2020arXiv200101409V](#), [2019ICRC...36.1016S](#)], future searches will be able to study neutrino emission from TDEs with much greater sensitivity. A measurement of O(\sim 1-10) TeV neutrinos without accompanying gamma rays would indicate that neutrino production is occurring in the X-ray photosphere, rather than in the UV photosphere. Indeed, such a detection would confirm the presence of a hidden X-ray source in the first place, while our electromagnetic observations cannot. Conversely, a lack of complementary low-energy neutrinos and gamma rays implies that only UV photons serve as a target. Neutrinos can uniquely serve as probes of the inner region of TDEs, using this novel method of extragalactic neutrino tomography. Now that a persistent central engine has been revealed in coincidence with a high-energy neutrino, we can begin to shed light on the role of TDEs as astrophysical accelerators.

14 Overflow

“Without interpolation all science would be impossible.”

Henri Poincare, *Lady Windermere's Fan*, 18??

“In theory there is no difference between theory and practice. In practise, there is.”

Feynman, *Lady Windermere's Fan*, 18??

“A neutrino is not a big thing to be hit by. In fact it's hard to think of anything much smaller by which one could reasonably hope to be hit. And it's not as if being hit by neutrinos was in itself a particularly unusual event for something the size of the Earth. Far from it. It would be an unusual nanosecond in which the Earth was not hit by several billion passing neutrinos.”

Douglas Adams, *The Hitchiker's Guide to the Galaxy*, 18??

14.1 Introduction

“Begin at the beginning,” the King said, gravely, “and go on till you come to an end; then stop.”

Lewis Carroll, *Alice in Wonderland*, 1899

14.1 Introduction	77
14.2 Neutrino Theory	78
14.3 The Zwicky Transient Facility (ZTF)	78
14.4 Event Selection	78
Event Reconstruction	78
Angular Errors	78
14.5 Unbinned Likelihood Analysis Formalism	78
14.6 Results	78
14.7 Diffuse Astrophysical Neutrino Flux	78
14.8 Neutrinos from Optical Transients	78
The Plot	78
14.9 Summary and Future Outlook	79

14.2 Neutrino Theory

“Though this be madness, yet there is method in it.”

William Shakespeare, *Hamlet*, 1556

glashow

14.3 The Zwicky Transient Facility (ZTF)

“We are all in the gutter, but some of us are looking at the stars”

Oscar Wilde, *Lady Windermere's Fan*, 18??

14.4 Event Selection

Event Reconstruction

Angular Errors

14.5 Unbinned Likelihood Analysis Formalism

“A hypothesis may be simply defined as a guess. A scientific hypothesis is an intelligent guess.”

Isaac Asimov, *Lady Windermere's Fan*, 18??

Cosmology + The PLOT

14.6 Results

14.7 Diffuse Astrophysical Neutrino Flux

14.8 Neutrinos from Optical Transients

The Plot

sensitivity versus depth Alerts vs ZTF

14.9 Summary and Future Outlook

“ FUTURE, *n.* That period of time in which our affairs prosper, our friends are true and our happiness is assured.” //

Ambrose Bierce, *The Cynic's Dictionary*, 1906

APPENDIX

A

Heading on Level 0 (chapter)

Hello, here is some text without a meaning. This text should show what a printed text will look like at this place. If you read this text, you will get no information. Really? Is there no information? Is there a difference between this text and some nonsense like "Huardest gef-burn"? Kjift – not at all! A blind text like this gives you information about the selected font, how the letters are written and an impression of the look. This text should contain all letters of the alphabet and it should be written in of the original language. There is no need for special content, but the length of words should match the language.

A.1 Heading on Level 1 (section)

Hello, here is some text without a meaning. This text should show what a printed text will look like at this place. If you read this text, you will get no information. Really? Is there no information? Is there a difference between this text and some nonsense like "Huardest gef-burn"? Kjift – not at all! A blind text like this gives you information about the selected font, how the letters are written and an impression of the look. This text should contain all letters of the alphabet and it should be written in of the original language. There is no need for special content, but the length of words should match the language.

Heading on Level 2 (subsection)

Hello, here is some text without a meaning. This text should show what a printed text will look like at this place. If you read this text, you will get no information. Really? Is there no information? Is there a difference between this text and some nonsense like "Huardest gef-burn"? Kjift – not at all! A blind text like this gives you information about the selected font, how the letters are written and an impression of the look. This text should contain all letters of the alphabet and it should be written in of the original language. There is no need for special content, but the length of words should match the language.

Heading on Level 3 (subsubsection)

Hello, here is some text without a meaning. This text should show what a printed text will look like at this place. If you read this text,

you will get no information. Really? Is there no information? Is there a difference between this text and some nonsense like "Huardest gefburn"? Kjift – not at all! A blind text like this gives you information about the selected font, how the letters are written and an impression of the look. This text should contain all letters of the alphabet and it should be written in of the original language. There is no need for special content, but the length of words should match the language.

Heading on Level 4 (paragraph) Hello, here is some text without a meaning. This text should show what a printed text will look like at this place. If you read this text, you will get no information. Really? Is there no information? Is there a difference between this text and some nonsense like "Huardest gefburn"? Kjift – not at all! A blind text like this gives you information about the selected font, how the letters are written and an impression of the look. This text should contain all letters of the alphabet and it should be written in of the original language. There is no need for special content, but the length of words should match the language.

A.2 Lists

Example for list (itemize)

- ▶ First item in a list
- ▶ Second item in a list
- ▶ Third item in a list
- ▶ Fourth item in a list
- ▶ Fifth item in a list

Example for list (4*itemize)

- ▶ First item in a list
 - First item in a list
 - * First item in a list
 - First item in a list
 - Second item in a list
 - * Second item in a list
 - Second item in a list
- ▶ Second item in a list

Example for list (enumerate)

1. First item in a list
2. Second item in a list
3. Third item in a list
4. Fourth item in a list
5. Fifth item in a list

Example for list (4*enumerate)

1. First item in a list
 - a) First item in a list
 - i. First item in a list
 - A. First item in a list
 - B. Second item in a list
 - ii. Second item in a list
- b) Second item in a list

Example for list (description)

First item in a list

Second item in a list

Third item in a list

Fourth item in a list

Fifth item in a list

Example for list (4*description)

First item in a list

Second item in a list

Greek Letters with Pronunciation

Character	Name	Character	Name
α	alpha <i>AL-fuh</i>	ν	nu <i>NEW</i>
β	beta <i>BAY-tuh</i>	ξ, Ξ	xi <i>KSIGH</i>
γ, Γ	gamma <i>GAM-muh</i>	\omicron	omicron <i>OM-uh-CRON</i>
δ, Δ	delta <i>DEL-tuh</i>	π, Π	pi <i>PIE</i>
ϵ	epsilon <i>EP-suh-lon</i>	ρ	rho <i>ROW</i>
ζ	zeta <i>ZAY-tuh</i>	σ, Σ	sigma <i>SIG-muh</i>
η	eta <i>AY-tuh</i>	τ	tau <i>TOW (as in cow)</i>
θ, Θ	theta <i>THAY-tuh</i>	υ, Υ	upsilon <i>OOP-suh-LON</i>
ι	iota <i>eye-OH-tuh</i>	ϕ, Φ	phi <i>FEE, or FI (as in hi)</i>
κ	kappa <i>KAP-uh</i>	χ	chi <i>KI (as in hi)</i>
λ, Λ	lambda <i>LAM-duh</i>	ψ, Ψ	psi <i>SIGH, or PSIGH</i>
μ	mu <i>MEW</i>	ω, Ω	omega <i>oh-MAY-guh</i>

Capitals shown are the ones that differ from Roman capitals.

Alphabetical Index

\sidecite, 17

glossary, 17

index, 17

citations, 17

hyperreferences, 18

nomenclature, 18